Cell Reports

Article

The endocytic adaptor AP-2 maintains Purkinje cell function by balancing cerebellar parallel and climbing fiber synapses

Graphical abstract

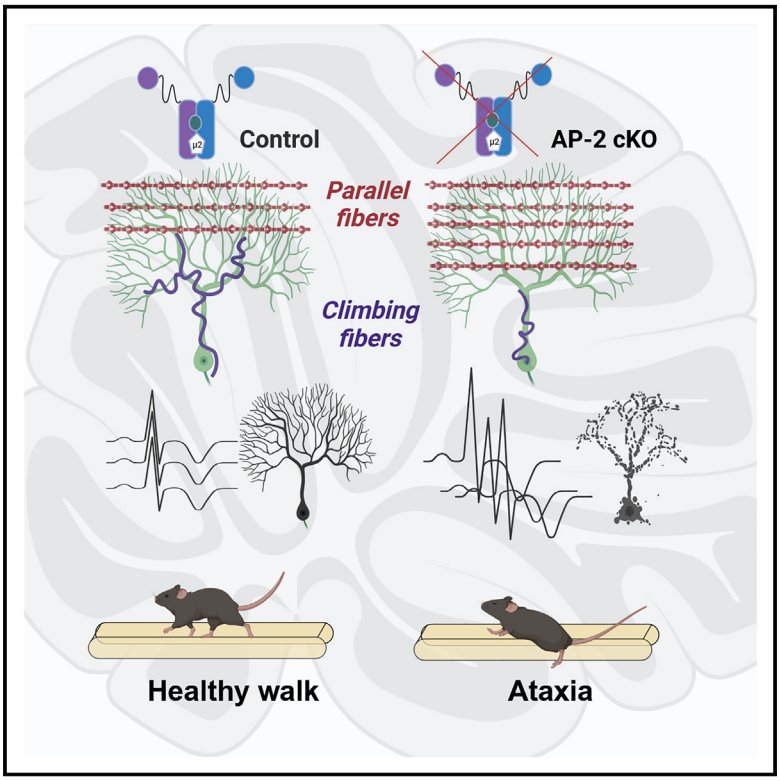

Authors

Marianna Tolve, Janine Tutas, Ebru Özer-Yildiz, ..., Silvana Valtcheva, Graziana Gatto, Natalia L. Kononenko

Correspondence

n.kononenko@uni-koeln.de

In brief

Tolve et al. demonstrate that AP-2 stabilizes GRID2IP to regulate synaptic function in Purkinje cells. Loss of AP-2 disrupts synaptic connectivity, alters network activity, and impacts motor coordination. This study highlights the importance of AP-2 in cerebellar function and its implications for neurodegenerative disorders.

Highlights

- Endocytic adaptor AP-2 is a crucial regulator of synaptic connectivity in the cerebellum
- Loss of AP-2 in Purkinje cells disrupts GRID2IP stability and GLURδ2 localization
- AP-2 deletion causes excess PF synapses and a drastic reduction in CF synapses
- AP-2 dysfunction alters cerebellar network, drives neurodegeneration, and causes ataxia

Tolve et al., 2025, Cell Reports *44*, 115256
February 25, 2025
https://doi.org/10.1016/j.celrep.2025.115256

CellPress

Cell Reports

CellPress
OPEN ACCESS

Article

The endocytic adaptor AP-2 maintains Purkinje cell function by balancing cerebellar parallel and climbing fiber synapses

Marianna Tolve,[1,2] Janine Tutas,[1,2] Ebru Özer-Yildiz,[1,2] Ines Klein,[3] Anne Petzold,[4] Veronika J. Fritz,[1,2] Melina Overhoff,[1,2] Quinn Silverman,[3] Ellie Koletsou,[1] Filip Liebsch,[5] Guenter Schwarz,[5,6] Tatiana Korotkova,[1,4,6] Silvana Valtcheva,[4] Graziana Gatto,[3] and Natalia L. Kononenko[1,2,6,7,8,*]

[1]Cologne Excellence Cluster Cellular Stress Response in Aging-Associated Diseases (CECAD), University of Cologne, Cologne, Germany
[2]Center for Physiology and Pathophysiology, Faculty of Medicine and University Hospital Cologne, University of Cologne, Cologne, Germany
[3]Neurology Department, University Hospital of Cologne, University of Cologne, Cologne, Germany
[4]Institute for Systems Physiology, Faculty of Medicine and University Hospital Cologne, University of Cologne, Cologne, Germany
[5]Institute of Biochemistry, Department of Chemistry, University of Cologne, Cologne, Germany
[6]Center for Molecular Medicine Cologne (CMMC), Faculty of Medicine and University Hospital Cologne, University of Cologne, Cologne, Germany
[7]Institute of Genetics, Faculty of Mathematics and Natural Sciences, University of Cologne, Cologne, Germany
[8]Lead contact
*Correspondence: n.kononenko@uni-koeln.de
https://doi.org/10.1016/j.celrep.2025.115256

SUMMARY

The loss of cerebellar Purkinje cells is a hallmark of neurodegenerative movement disorders, but the mechanisms remain enigmatic. We show that endocytic adaptor protein complex 2 (AP-2) is crucial for Purkinje cell survival. Using mouse genetics, viral tracing, calcium imaging, and kinematic analysis, we demonstrate that loss of the AP-2 μ subunit in Purkinje cells leads to early-onset ataxia and progressive degeneration. Synaptic dysfunction, marked by an overrepresentation of parallel fibers (PFs) over climbing fibers (CFs), precedes Purkinje cell loss. Mechanistically, AP-2 interacts with the PF-enriched protein GRID2IP, and its loss triggers GRID2IP degradation and glutamate δ2 receptor (GLURδ2) accumulation, leading to an excess of PFs while CFs are reduced. The overrepresentation of PFs increases Purkinje cell network activity, which is mitigated by enhancing glutamate clearance with ceftriaxone. These findings highlight the role of AP-2 in regulating GRID2IP levels in Purkinje cells to maintain PF-CF synaptic balance and prevent motor dysfunction.

INTRODUCTION

Purkinje cells in the cerebellum play a vital role in motor learning and adaptation,[1–3] and their dysfunction or degeneration is a hallmark of neurodegenerative movement disorders with ataxic symptoms. Despite extensive research, the mechanisms governing Purkinje cell survival remain elusive. Deterioration of Purkinje cell function is often accompanied by changes in glutamatergic synapses. Alterations in glutamatergic transmission, particularly at the two primary excitatory inputs to Purkinje cells—climbing fiber (CF) synapses, originating from the inferior olive, and parallel fiber (PF) synapses, composed of the axons of the granule cells[4]—are common in spinocerebellar ataxia (SCA).[5–10] Loss of CFs often precedes Purkinje cell degeneration[10] and is accompanied by the strengthening of PF synapses, a process known as heterosynaptic competition.[11–13] Given that CFs and PFs innervate distinct regions of the dendritic arbors, with CFs targeting proximal and PFs distal dendrites of Purkinje cells, the loss of one fiber type leads to an increase in the other.[14–16] Maintaining the delicate balance between CF and PF synaptic inputs is crucial for synaptic plasticity and cerebellar gain control.[17] However, the precise mechanisms governing the maintenance of this balance and its relationship to Purkinje cell degeneration remain poorly understood. A particularly intriguing question is whether the regulation of CF and PF synaptic balance occurs in a Purkinje cell autonomous manner.

A variety of signaling cascades at the plasma membrane, including receptor signaling,[18,19] ion channels,[15,20–23] and cell adhesion molecules,[24] are proposed to regulate heterosynaptic competition between CF and PF synapses. Adaptor protein complex 2 (AP-2) is a major orchestrator of clathrin-mediated endocytosis (CME) at the plasma membrane.[25–27] AP-2 is comprised of four subunits: α, β, μ, and σ,[28] and a mutation in its core μ subunit has recently been associated with developmental encephalopathy with ataxia.[29] Although the role of AP-2 in cortical and hippocampal neurons has been extensively studied,[30–37] its function in the cerebellum, particularly in Purkinje cells, remains unexplored.

We report that AP-2 regulates cerebellar function by controlling PF and CF synaptic rewiring in a cell-autonomous manner. Mice lacking the AP-2 μ subunit in Purkinje cells exhibit early gait disturbances along with progressive Purkinje cell degeneration.

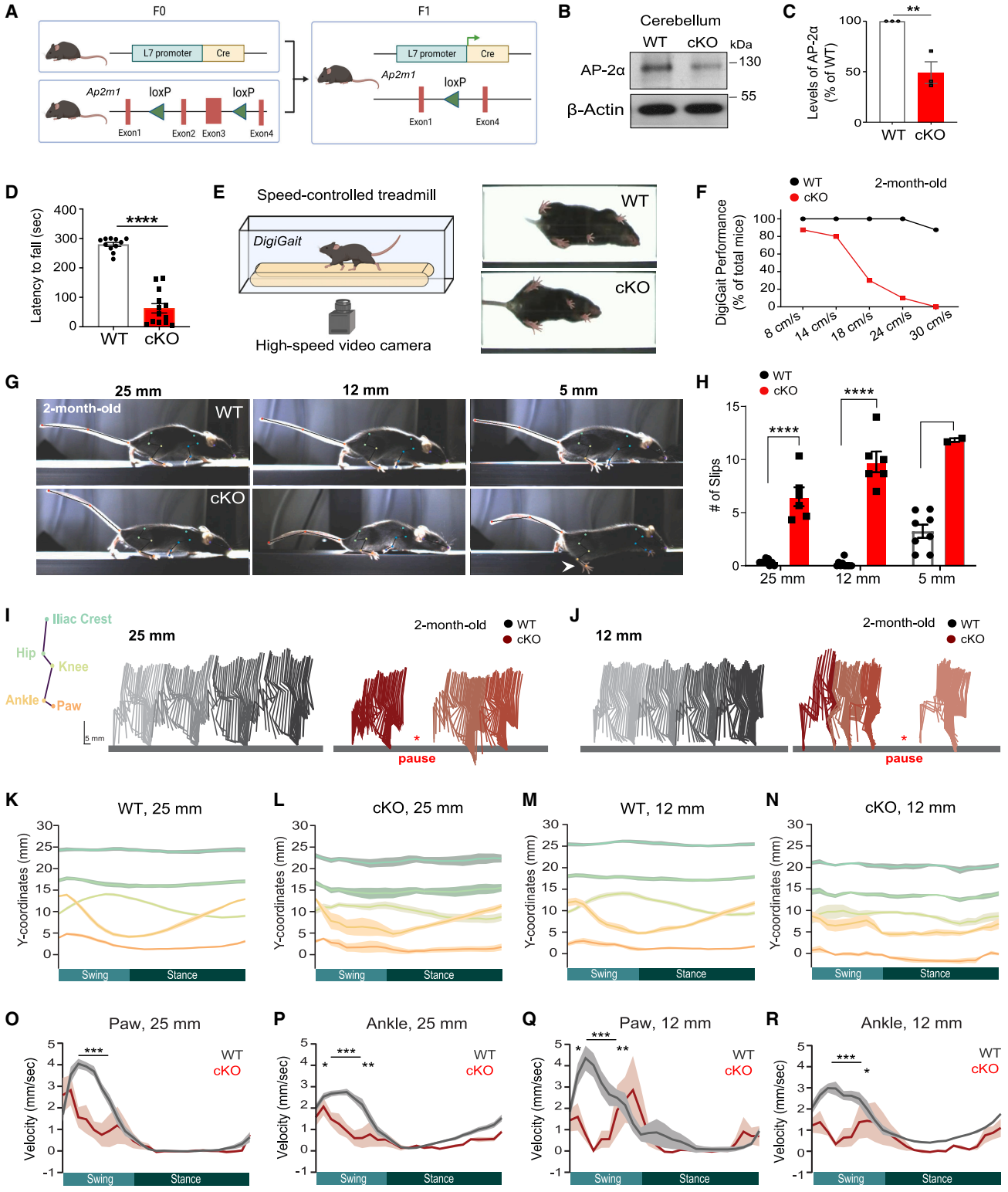

Figure 1. Loss of AP-2 in cerebellar Purkinje cells causes early ataxia in mice

(A) Schematic of AP-2 cKO mouse generation.

(B and C) Representative immunoblot (B) and analysis (C) of AP-2α levels in 2-month-old WT and AP-2 cKO cerebellar lysates. Each dot represents one mouse ($N = 3$ for each genotype). Statistical significance was determined by one-tailed unpaired t test ($p = 0.005$).

(legend continued on next page)

Increased numbers of dendritic spines and PF inputs precede Purkinje cell loss, while CFs are significantly reduced. Mechanistically, we demonstrate that AP-2 localizes to Purkinje cell dendrites, where it interacts with the PF synapse-enriched protein GRID2IP. Loss of AP-2 results in the proteasome-dependent degradation of GRID2IP and glutamate δ2 receptor (GLURδ2) accumulation, resulting in excess PF synapses. Our study suggests that the overrepresentation of PF synapses may contribute to increased Purkinje cell network activity, which is alleviated by enhancing glutamate clearance with the antibiotic ceftriaxone. While the causal link between synaptic rewiring and Purkinje cell degeneration remains uncertain, we propose that the early PF-CF imbalance underlies motor dysfunction in AP-2 conditional knockout (cKO) mice. Our study identifies a role of AP-2 in maintaining PF-CF synaptic balance and preventing gait dysfunction by regulating GRID2IP in the cerebellum.

RESULTS

Mice lacking the endocytic adaptor AP-2 in Purkinje cells exhibit severe and early ataxia

AP-2 is essential for CME, but its role in cerebellar Purkinje cells remains unexplored. We hypothesized that AP-2 is critical for motor coordination by regulating PF-CF synapse balance in Purkinje cells. To test this, we generated Purkinje cell-specific AP-2μ knockout (KO) mice (henceforth defined as AP-2 cKO mice) by crossing floxed *Ap2m1* mice[35] with L7/*Pcp2*-Cre mice, where Cre recombinase activity is fully established 2 weeks post birth[38] (Figure 1A). AP-2μ loss destabilizes the AP-2 complex, leading to subsequent degradation of its α subunits.[33] Successful recombination was confirmed by Ai9-tdTomato reporter expression (Figure S1A) and marked reduction of AP-2 in cKO mice, detected via western blot (Figures 1B and 1C) and immunohistochemistry (Figures S1B and S1C). Although *Ap2m1* is expressed in all cerebellar cell types, the two AP-2α isogenes (*Ap2a1* and *Ap2a2*) are highly enriched in Purkinje cells[39] (Figure S1D), enabling specific detection of AP-2 in Purkinje cells by western blot using the AP-2α antibody. Loss of AP-2 impaired CME functionality, evident from the absence of clathrin foci in Purkinje cell dendrites (Figure S1E) and reduced transferrin uptake in acute AP-2 cKO cerebellar slices (Figures S1F and S1G).

AP-2 cKO mice were viable but had reduced body weight by 2 months (Figures S1H and S1I), primarily due to reduced fat mass (Figure S1J). To test whether AP-2 is required in Purkinje cells for motor coordination, we subjected the wild-type (WT) (i.e., $Ap2m1^{wt/wt}$; $L7^{Cre}$) and AP-2 cKO (i.e., $Ap2m1^{fl/fl}$; $L7^{Cre}$) mice to classic motor tasks, including the rotarod, treadmill, and self-paced locomotion on narrow beams.[40,41] By 2 months, AP-2 cKO mice displayed severe motor deficits, including significantly reduced rotarod performance (Figure 1D) and impaired treadmill locomotion (Figures 1E and 1F; Videos S1 and S2). Of note, no gross locomotor problems were observed in mice younger than 2 months (data not shown). On wide beams (25 mm), AP-2 cKO mice slipped more frequently than WT controls (Figures 1G and 1H; Videos S3 and S4) and struggled on narrower beams (12 and 5 mm), rarely completing crossing of the 5-mm beam (Figure 1H; Videos S5, S6, S7, and S8).

Kinematic analysis using AutoGaitA[42] revealed altered limb kinematics in AP-2 cKO mice (Figures 1I and 1J). On the 25-mm beam, they exhibited reduced ankle and knee joint excursion and a lower iliac crest position (Figures 1K, 1L, S2A, S2B, S2D, S2F, S2H, and S2J), with these differences being more pronounced on the narrower 12-mm beam (Figures 1M, 1N, S2C, S2E, S2G, S2I, and S2K). Additionally, joint coordination was impaired, particularly in knee and ankle angles (Figures S2L–S2Q), while hip angles remained similar to those of controls (Figures S2R and S2S). Swing-phase speeds of paw and ankle movements were also significantly reduced on both beams (Figures 1O–1R; Table S1). These findings indicate that AP-2 is required in Purkinje cells for motor coordination, with AP-2 cKO mice showing lower limb incoordination akin to the ataxic gait observed in cerebellar dysfunction.[43,44]

Loss of Purkinje cells in AP-2 cKO mice is preceded by their increased spine density

Ataxic gait in patients is often linked to cerebellar atrophy,[45] while Purkinje cell loss causes ataxia in mice.[46] To explore the mechanism of gait dysfunction in AP-2 cKO mice, we analyzed cerebellar morphology and Purkinje cell numbers. Immunohistochemical analysis of 2-month-old AP-2 cKO cerebella revealed no gross cerebellar changes but a marked reduction in Purkinje cell number (Figure 2A), confirmed by Nissl staining of cerebellar slices (Figures 2B–2D and S3A–S3C). Purkinje cell loss was not

(D) Rotarod performance of 2-month-old WT and AP-2 cKO mice. Each dot represents one mouse ($N = 11$ for WT; $N = 13$ for cKO). Statistical significance was determined by unpaired two-tailed Student's t test ($p < 0.0001$).
(E and F) Ambulation of 2-month-old WT and AP-2 cKO mice on a translucent treadmill (DigiGait) at controlled speeds (from 8 to 30 cm/s).
(E) Schematic illustrating the DigiGait setup used to monitor mice locomotion while running on a speed-controlled treadmill. Created in BioRender.
(F) The percentage of mice able to ambulate at the indicated speeds (8 cm/s: WT $N = 3$, cKO $N = 8$; 14–30 cm/s: WT $N = 6$, cKO $N = 10$).
(G) Example images of WT and AP-2 cKO mice crossing beams of different widths (25, 12, and 5 mm). The white arrow indicates the slip of an AP-2 cKO mouse.
(H) Quantification of slips in 2-month-old WT and AP-2 cKO mice crossing beams of different widths (25 mm: $p < 0.0001$; 12 mm: $p < 0.0001$; 5 mm: $p < 0.0001$). Each dot represents one mouse (25 and 12 mm: $N = 9$ for WT, $N = 6$ for cKO; 5 mm: $N = 9$ for WT, $N = 2$ for cKO). cKO mice drop out on the 5-mm beam.
(I and J) Stick diagrams representing hindlimb kinematics during a step cycle in WT and AP-2 cKO mice crossing 25-mm (I) or 12-mm (J) beams. Kinematic analysis in AP-2 cKO mice was limited to these beams due to frequent slips and falls on the 5-mm beam.
(K–N) Line graphs showing variations in the height (y coordinates) of the iliac crest, hip, knee, ankle, and hindpaw during a normalized step cycle on a 25-mm-wide (K and L) or 12-mm-wide (M and N) beams (25 and 12 mm: $N = 9$ for WT, $N = 6$ for cKO).
(O–R) Line graphs showing variations in hindpaw (O and Q) and ankle (P and R) velocities during a normalized step cycle on the 25-mm (O and P) and 12-mm (Q and R) beams ($N = 9$ for WT, $N = 6$ for cKO).
Data are presented as mean ± SEM. Statistical significance in (H) and (O)–(R) was determined by two-way ANOVA followed by Šidák multiple-comparisons test. (K)–(R) display mean values as dark lines and SEM as shaded areas. $^{*}p \leq 0.05$, $^{**}p \leq 0.01$, $^{***}p \leq 0.001$, $^{****}p \leq 0.0001$.

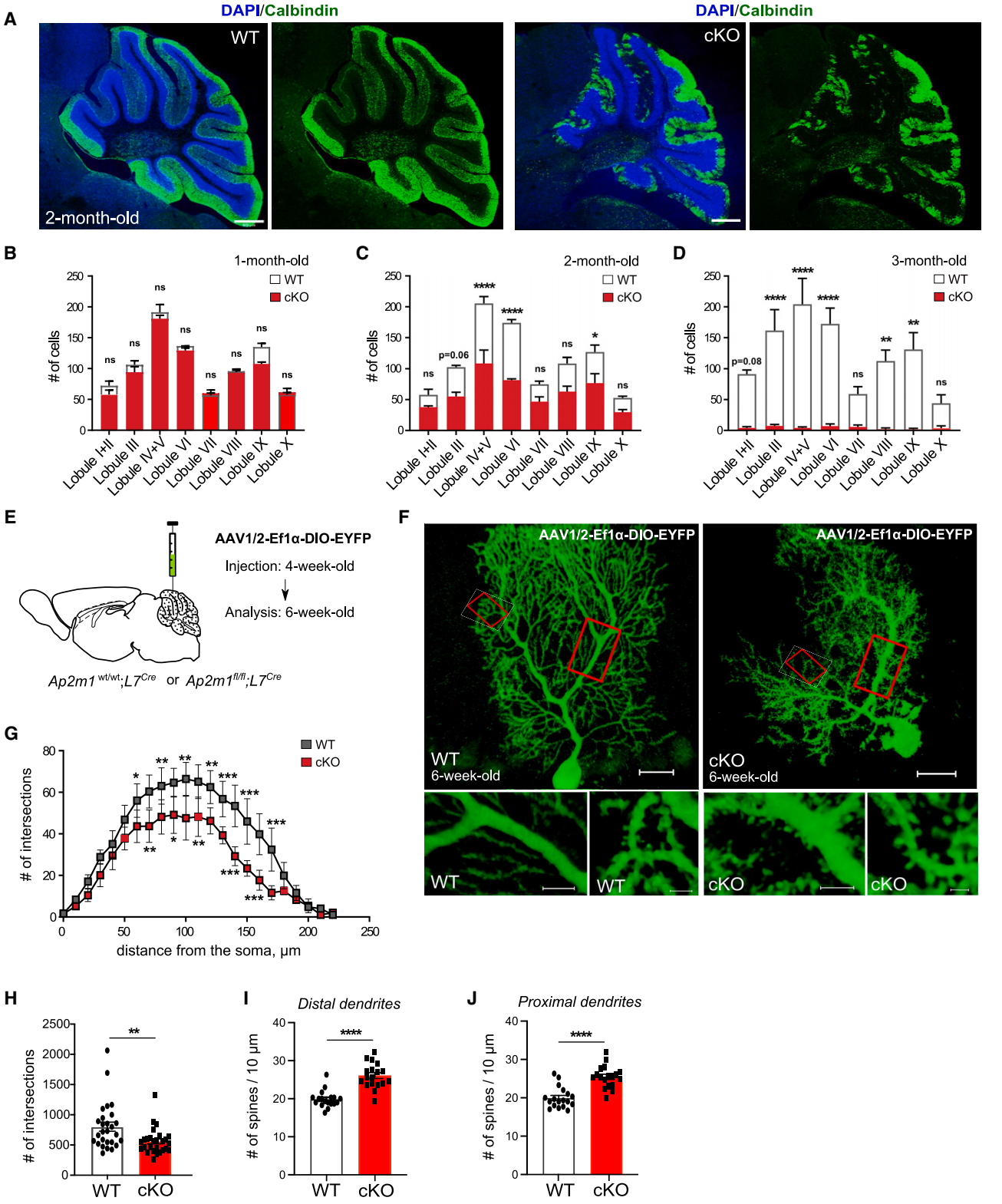

(legend on next page)

due to developmental effects, as Purkinje cells were still present in the 1-month-old AP-2 cKO cerebellum (Figure 2B), and was progressive, with nearly all AP-2-deficient Purkinje cells being lost by 3 months of age (Figures 2D and S3D).

To take a detailed look at Purkinje cell morphology at the onset of degeneration, we stereotactically delivered an adeno-associated virus (AAV) carrying EYFP flanked by double-inverted orientation (DIO) sites (AAV1/2-Ef1α-DIO-EYFP), allowing Cre-dependent expression, into the cerebellum of 4-week-old WT (*Ap2m1*$^{wt/wt}$;L7^{Cre}) and AP-2 cKO (*Ap2m1*$^{fl/fl}$;L7^{Cre}) mice (Figure 2E). Analysis of 6-week-old EYFP-expressing Purkinje cells in AP-2 cKO mice revealed only subtle changes in their branching pattern (Figures 2F–2H). Surprisingly, however, these Purkinje cells exhibited a significant increase in spine-like protrusions along both proximal and distal dendrites (Figures 2I and 2J; see also Figure 2F). This increase in spine density was likely independent of the canonical role of AP-2 in CME, as it was not observed in cultured Purkinje cells treated with the clathrin inhibitor PitStop2 (Figures S3E–S3I). These data provide the first line of evidence that synaptic dysfunctions may precede cell death and gait abnormalities in AP-2 cKO mice.

AP-2-deficient Purkinje cells reveal proteome alterations at glutamatergic synapses

To further explore how precisely AP-2 functions in Purkinje cells to support motor coordination, we conducted quantitative mass spectrometry (MS) analysis of WT and AP-2 cKO cerebella before (1 month old) and during (2 months old) the "cell death" window. At 1 month, only a few proteins were altered (Figure 3A), whereas more pronounced changes were observed at 2 months (Figure 3B; Table S2). Notably, half of the proteins altered at 1 month overlapped with those altered in 2-month-old AP-2 cKO cerebella (Figure S4A). Gene Ontology (GO) analysis of upregulated proteins at 1 month highlighted "glutamatergic synapse" as a key component (Figure 3C), suggesting that synaptic changes precede Purkinje cell degeneration. At 2 months, downregulated proteins were associated with "postsynapse" and "glutamatergic synapses" (Figure 3D), while upregulated proteins were linked to "neuronal death" and "microglia activation" (Figure 3E), which aligns with the onset of Purkinje cell loss observed at this age. Furthermore, the upregulation of apoptotic caspase-3 and -6 in the 2-month-old AP-2 cKO proteome and in AP-2 cKO Purkinje cells (Figures 3B, S4B, and S4C) suggests that these cells undergo cell death by apoptosis. Consistent with our behavioral data (Figure 1), we observed that many downregulated proteins in the cerebellum of 2-month-old AP-2 cKO mice were associated with SCA (Figure 3F).

To investigate proteome alterations specifically in Purkinje cells, we employed proximity labeling with dimerized ascorbate peroxidase (dAPEX2). We stereotactically delivered an AAV carrying a cytosolic version of dAPEX2 flanked by DIO (ssAAV-1/2-hEF1α-DIO-dAPEX2) into the 6-week-old cerebellum of WT (i.e., *Ap2m1*$^{wt/wt}$;L7^{Cre}) and AP-2 cKO (i.e., *Ap2m1*$^{fl/fl}$; L7^{Cre}) mice to enable Purkinje cell-dependent expression of APEX2 (Figure 3G). In the presence of hydrogen peroxide, APEX biotinylates nearby proteins, which are then enriched using streptavidin beads and identified by MS. Three weeks after injection, significant enrichment of streptavidin-labeled proteins was observed in acute cerebellar slices (Figure S4D). Proteomic analysis revealed that many proteins were downregulated in Purkinje cells lacking AP-2 compared to the WT (Figure 3H; Table S3), primarily involved in "actin filament organization" and "synapse organization" (Figure 3I). Additionally, key players of CME, such as DMN3, CLTC, SH3GL2, and DNAJC6, were significantly decreased (Figure 3J), confirming the validity of our approach. In agreement with this, deletion of AP-2 led to increased surface levels of the vesicular gamma-aminobutyric acid (GABA) transporter and decreased synaptotagmin 1 uptake (Figures S4E–S4I), both of which require AP-2 for proper recycling from the plasma membrane.[33,47] FM1-43 dye uptake was also slowed in Purkinje cells lacking AP-2 (Figures S4J–S4M), further supporting the notion of impaired endocytosis in these cells.[26] When comparing downregulated proteins in the whole cerebellum to the Purkinje cell-enriched proteome, we found that about a quarter of cerebellar proteins were specifically reduced in Purkinje cells (Figures 3K and 3L). Many of these proteins were associated with SCA and glutamatergic synapses (Figure 3L). These comprehensive proteomic analyses show that AP-2 deletion in Purkinje cells not only impairs endocytosis but also disrupts glutamatergic synaptic pathways.

AP-2 regulates the stability of the PF synapse-enriched protein GRID2IP

Given the alterations in glutamatergic synaptic pathways, we next investigated the interactome of AP-2 in Purkinje cells through MS-based analysis using the AP-2α antibody as bait

Figure 2. Increased spine density precedes progressive loss of AP-2 cKO Purkinje cells

(A) Representative confocal images of WT and AP-2 cKO cerebella immunostained for calbindin. Scale bars: 500 μm.

(B–D) Quantification of Purkinje cell number via Nissl staining (Figures S3A–S3C) in 1-month-old (B), 2-month-old (C), and 3-month-old (D) WT and AP-2 cKO mice (N = 3 per genotype and age). Statistical significance was determined by two-way ANOVA followed by Tukey's multiple comparisons (2 months: lobule IV/V $p < 0.0001$; lobule VI $p < 0.0001$; lobule IX $p = 0.041$. 3 months: lobule III $p < 0.0001$; lobule IV/V $p < 0.0001$; lobule VI $p < 0.0001$; lobule VIII $p < 0.0001$; lobule IX $p = 0.0011$).

(E and F) AAV1/2-Ef1α-DIO-EYFP injection timeline (E) and representative confocal images (F) of EYFP-transduced WT and AP-2 cKO Purkinje cells. Scale bars: 20 μm; right inset, 5 μm; left inset, 2 μm.

(G) Sholl analysis of EYFP-transduced WT and AP-2 cKO Purkinje cells (N = 5 mice for WT, N = 3 mice for cKO). Statistical significance was determined by two-way ANOVA followed by Tukey's multiple comparisons (p values can be found in the source data).

(H) Total intersections in EYFP-transduced WT and AP-2 cKO Purkinje cells. Each dot represents one cell (WT: n = 27 cells from N = 5 mice; cKO: n = 27 cells from N = 3 mice). Statistical significance was determined by unpaired two-tailed Student's t test ($p = 0.006$).

(I and J) Spine density in proximal (I) and distal (J) dendrites of EYFP-transduced WT and AP-2 cKO Purkinje cells. Each dot represents one cell (n = 18 cells, N = 3 mice per genotype). Statistical significance was determined by unpaired two-tailed Student's t test (proximal dendrites: $p < 0.0001$; distal dendrites: $p < 0.0001$) Data are presented as mean ± SEM. *$p \leq 0.05$, **$p \leq 0.01$, ***$p \leq 0.001$, ****$p \leq 0.0001$. n.s., non-significant.

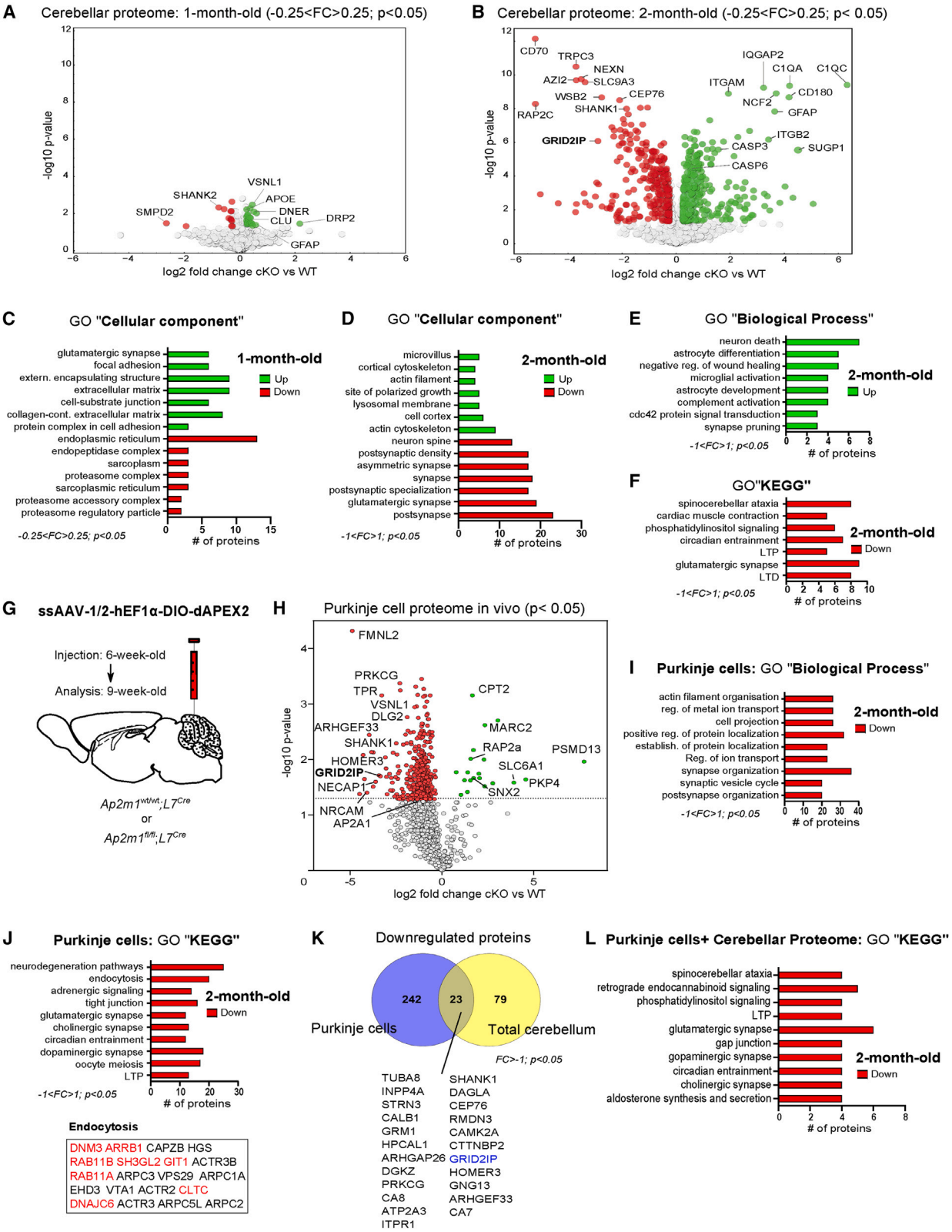

(legend on next page)

(Figure 4A; Table S4). Next to pulling down components of the AP-2 complex and known AP-2 binding partners (i.e., STON2, CLTB, and PICALM), we identified GRID2IP (also known as Delphilin). GRID2IP was one of the 15 proteins that interacted with AP-2α in our MS pull-down experiments and was downregulated in AP-2 cKO Purkinje cells (Figure 4B). GRID2IP is a PDZ and formin homology (FH) domain-containing protein selectively expressed in Purkinje cells.[48] The FH domains are known to promote filamentous actin nucleation, while PDZ domains are typically found in scaffold proteins at postsynaptic membranes. Biochemical and immunohistochemical experiments confirmed that AP-2 and GRID2IP interact and colocalize in Purkinje cell dendrites (Figures 4C–4E). In AP-2 cKO mice, GRID2IP levels were significantly reduced both in cerebellar lysates (Figures 4F and 4G) and Purkinje cells (Figure 4H). To map the distribution of GRID2IP on Purkinje cells in 3D, we reconstructed dendritic trees of 6-week-old WT and AP-2 cKO Purkinje cells transduced with AAV-EYFP-DIO (Figure 2E). The density of GRID2IP distribution was significantly reduced in AP-2 cKO Purkinje cells compared to controls (Figures 4I and 4J). This reduction was not due to a decrease in its mRNA expression (Figures 4K and 4L), suggesting that AP-2 regulates GRID2IP protein stability. The ubiquitin-proteasome system is a central player in regulating turnover of cytoplasmic proteins, including the degradation of a homologous formin protein, mDia2.[49] To test whether GRID2IP is more susceptible to proteasomal degradation in the absence of AP-2, we incubated WT and AP-2 cKO acute cerebellar slices with the proteasome inhibitor MG132. Indeed, a 6.5-h treatment with MG132 was sufficient to increase GRID2IP levels in WT Purkinje cells and restore its normal expression in Purkinje cells lacking AP-2 (Figures 4M and 4N), suggesting that the binding of AP-2 to GRID2IP might be required to protect GRID2IP from proteasome degradation.

AP-2 loss causes GLURδ2 accumulation and PF-CF synapse imbalance

Our identified interaction between AP-2 and the postsynaptic scaffolding protein GRID2IP (Figure 5A) prompted us to investigate its potential impact on cerebellar synaptic organization. Since GRID2IP interacts with the glutamate δ2 receptor (GLURδ2, also known as GluD2, encoded by the *GRID2* gene),[48] an orphan glutamate receptor expressed at PF-Purkinje cell synapses,[50,51] we first analyzed GLURδ2 levels at WT and AP-2 cKO PF synapses identified by their VGLUT1 expression.[52] GLURδ2 levels were upregulated in 1-month-old AP-2 cKO Purkinje cells (before Purkinje cell loss) (Figures 5B–5D) and remained elevated at 6 weeks (Figure S5A). Although GLURδ2 lacks channel activity, it has a synaptogenic role at PFs, binding cerebellin-1 secreted by granule cells,[53,54] which, in turn, interacts with presynaptic neurexin[55] (Figure 5A). GLURδ2 KO mice exhibit motor learning deficits[56,57] and reduced PF synapses,[20,58] while its overexpression causes PF overgrowth and spine-like protrusions.[59] Given the accumulation of GLURδ2 at AP-2 cKO PF synapses, we speculated that this drives increased PF formation. 3D analysis of VGLUT1-positive PF synapses revealed a significant increase in PF synapse density in 6-week-old AP-2 cKO mice (Figures 5E, 5F, and 5I), detectable as early as 1 month (Figures S5B and S5C). This aligns with the early dysfunction at glutamatergic synapses described above (Figure 3C). This increase in PF synapses coincided with a near-complete loss of CF synapses (Figures 5G, 5H, and 5J) and perisomatic CF accumulation (Figures 5K and 5L). Since AP-2 is deleted specifically in Purkinje cells (Figures S1B, S1C, and S3D) and not in inferior olive neurons forming CFs (Figures S5D–S5G), these finding indicate a cell-autonomous role of AP-2 in refining PF/CF synaptic inputs.

AP-2 balances PF and CF synapses during development but not in the adult brain

To determine when AP-2 activity is crucial for controlling the balance between PF and CF synaptic inputs, we considered the developmental timeline of CF innervation in Purkinje cells. At birth, Purkinje cell somata are innervated by multiple CFs,[12] but during early postnatal development, supernumerary CFs regress and translocate from the somata to dendrites, a process completed by post-natal day 21.[60–63] Our data suggest that AP-2 regulates PF formation and that its loss disrupts CF translocation, leading to an overabundance of PF synapses (Figure 6A). If AP-2 is required only during early development for CF translocation, then its deletion after post-natal day 21 should not affect CF translocation, as the CF territory is already established. To test this, we first analyzed CF density in 1-month-old AP-2 cKO mice. We found that AP-2 deletion during early postnatal development (as L7-Cre recombinase is fully active by 2 weeks after birth) resulted in a large increase in the number of perisomatic CFs, a phenotype consistent with their failure to translocate to the Purkinje cell dendrites (Figures 6B and 6C). Next, we tested whether acute deletion of AP-2 in mature Purkinje cells affects CF density by stereotactically injecting an AAV

Figure 3. Proteomics reveals glutamatergic synapse alterations in AP-2 cKO cerebellum

(A and B) Volcano plots showing differentially expressed proteins in cerebellar lysates of WT and AP-2 cKO mice at 1 month (A) and 2 months (B) of age. Red and green circles mark significantly upregulated and downregulated proteins, respectively. *N* = 5 per genotype.

(C and D) GO analysis of "cellular component"-enriched terms in the cerebella of 1-month-old (C) and 2-month-old AP-2 cKO mice (D).

(E) GO analysis of "biological process"-enriched terms in the cerebella of 2-month-old AP-2 cKO mice.

(F) GO analysis of "Kyoto Encyclopedia of Genes and Genomes (KEGG)"-enriched terms in the cerebella of 2-month-old AP-2 cKO mice.

(G) ssAAV-1/2-hEF1α-DIO-dAPEX2 injection timeline.

(H) Volcano plot of differentially expressed proteins in dAPEX2-transduced WT and AP-2 cKO Purkinje cells. Red and green circles mark significant upregulation and downregulation, respectively. *N* = 2 per genotype.

(I) ShinyGo v.0.80-based GO analysis of downregulated biological process-enriched terms in AP-2 cKO Purkinje cells.

(J) GO analysis of KEGG-enriched terms in AP-2 cKO Purkinje cells. Bottom: downregulated proteins within the term "endocytosis." Known AP-2 binding partners are indicated in red.

(K) Venn diagram illustrating commonly downregulated proteins in the total cerebellar proteome and APEX2-transduced AP-2 cKO Purkinje cells.

(L) GO analysis of commonly downregulated KEGG-enriched terms in the cerebellar proteome and APEX2-transduced AP-2 cKO Purkinje cells.

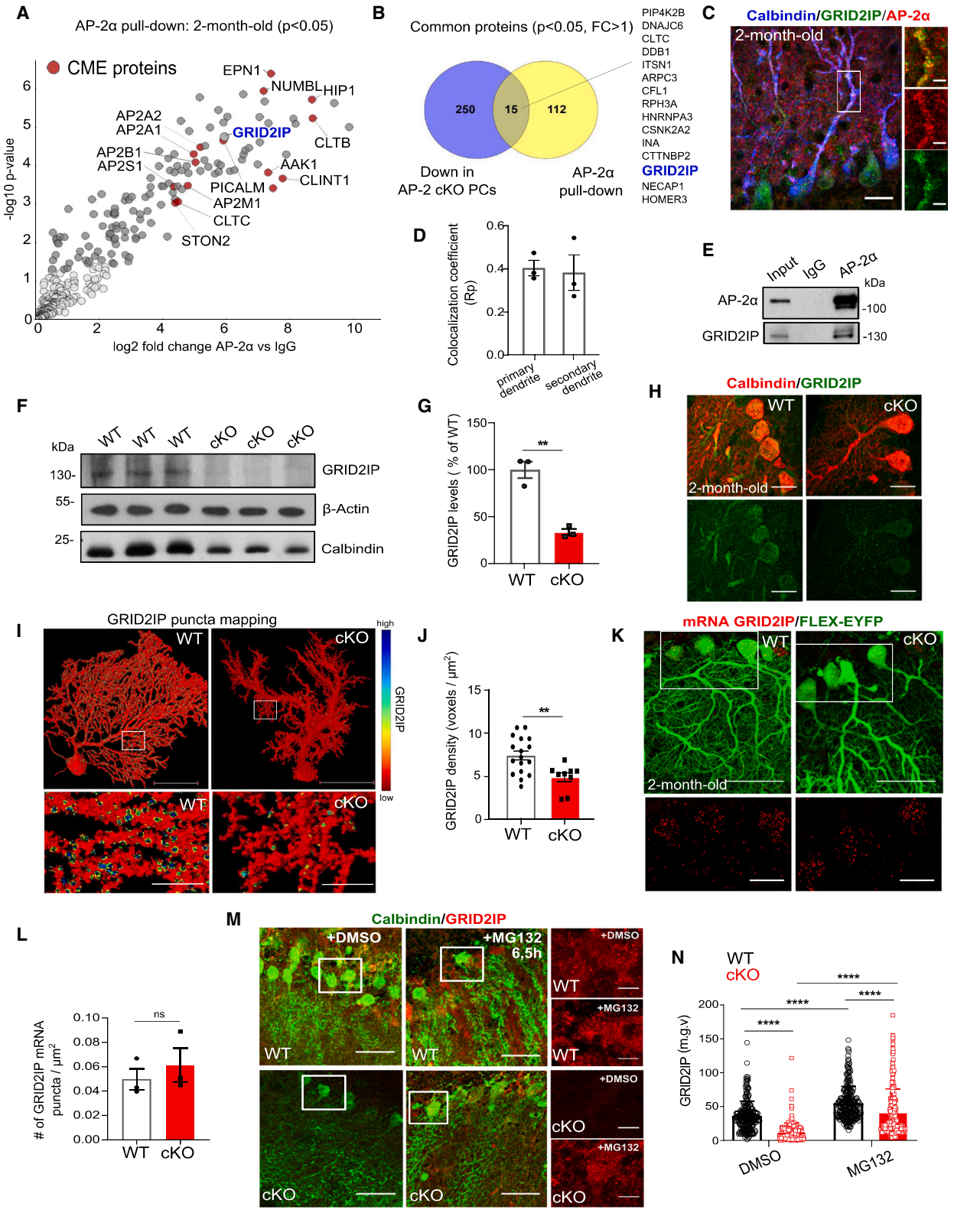

(legend on next page)

expressing L7-driven EYFP and Cre-recombinase into 6-week-old *Ap2m1* flox/flox mice (Figure 6D). At 10 weeks, AP-2-deficient Purkinje cells (Figures S5H and S5I) showed no changes in morphology (Figure 6E), spine density (Figure 6F), PF/CF territory (Figures 6G–6J), or GLURδ2 levels (Figures 6K and 6L). Although only a limited number of Purkinje cells were targeted using this approach, these results suggest that AP-2 is essential for balancing PF-CF synapses during early postnatal cerebellar development but that is not required for maintaining this balance in mature Purkinje cells.

Activity-dependent potentiation of Purkinje cell network activity without AP-2

Finally, we examined whether the PF/CF input imbalance impacts Purkinje cell network activity in AP-2 mice. First, we evaluated the intrinsic electrophysiological properties of Purkinje cells in acute cerebellar slices. At 1 month, AP-2-deficient Purkinje cells showed unaltered baseline electrophysiological properties (Figures 7A, 7B, and S6A–S6C) but required higher current injection to elicit action potentials (Figure 7C; Table S5). Next, we assessed the network output of WT and AP-2 cKO Purkinje cells during 100 Hz stimulation, a physiologically relevant frequency for motor learning.[64] Using GCaMP7f-based live imaging in organotypic cerebellar slices prepared on postnatal day 8 and imaged on day in vitro 21 (prior to Purkinje cell degeneration), we recorded their synaptic responses (Figures 7D and 7E). Both the average response to stimulation and the peak amplitude of responses were significantly elevated in AP-2 cKO Purkinje cells compared to the WT (Figures 7F, 7G, and S6D). Moreover, Ca^{2+} transients in AP-2 cKO Purkinje cells were markedly increased within 1–10 s post stimulation (Figure 7H) and remained elevated up to 20 s after stimulation (Figure 7I). This was accompanied by a delayed average time to reach the maximal peak response (Figures 7J and S6E), likely attributed to the presence of a second, lower-amplitude peak of Ca^{2+} transients (Figure 7G). These findings suggest heightened recurrent activity in AP-2 cKO Purkinje cells despite reduced stereotypy of neuronal responses (Figures 7K and 7L). Importantly, the density of Bergmann glia, which can modulate Purkinje cell activity by regulating extracellular glutamate spillover,[65] was not significantly altered in AP-2 cKO cerebella (Figures S6F–S6H). Collectively, these data demonstrate that AP-2 deletion causes asynchronous firing and increased network output of Purkinje cells.

To determine whether the heightened Purkinje cell network activity in AP-2 cKO mice is driven by increased synaptic input from excessive PF synapses, we treated organotypic slices with ceftriaxone, a β-lactam antibiotic known to enhance synaptic glutamate reuptake by upregulating the glial glutamate transporter GLT-1[66] (Figures 7M–7O). GLT-1, expressed in Bergmann glia,[67] is neuroprotective in various excitotoxicity models.[66,68,69] After 7 days of ceftriaxone treatment, GLT-1 levels were elevated in the cerebellum (Figures S6I and S6J), and Purkinje cell network activity in AP-2 cKO slices was markedly reduced (Figures 7P, 7Q, and S6K). However, peak response in AP-2 cKO cells persisted (Figure 7S), likely due to the excess perisomatic CF synapses (Figure 6L). Furthermore, ceftriaxone treatment reduced the stereotypicity of stimulus-evoked responses in AP-2 cKO cells, resulting in an almost 3-fold decrease compared to WT cells (Figures 7T and 7U). Of note, GLT1 levels were unaltered in cerebellar lysates from AP-2 cKO mice (Figures S6L and S6M). The limited effect of ceftriaxone on WT Ca^{2+} activity at 1–10 s post stimulation (Figure 7Q) likely reflects the predominant role of GLAST over GLT-1 in glutamate clearance under physiological conditions.[70]

Finally, to assess whether increased network output drives Purkinje cell loss in AP-2 cKO mice, we treated 1-month-old organotypic slices with ceftriaxone for 2 weeks and then analyzed Purkinje cell numbers. Ceftriaxone treatment restored the number of Purkinje cells in AP-2 cKO slices (Figures S6N and S6O). These findings suggest that early PF/CF input rewiring in AP-2 cKO Purkinje cells is associated with heightened network output and that enhancing synaptic glutamate reuptake normalizes network excitation. The exacerbation of asynchronous firing of AP-2 cKO Purkinje cells after ceftriaxone treatment (Figure7U) is likely due to the loss of dendritic CFs in these mice, consistent

Figure 4. GRID2IP is a binding partner of AP-2 in the cerebellum

(A) Volcano plot showing AP-2α pull-down interactors from 2-month-old WT cerebellum ($N = 5$) identified by MS. Gray circles mark proteins significantly enriched over the immunoglobulin G (IgG) control; red highlights known CME binding partners.

(B) Venn diagram of significantly downregulated proteins in AP-2 cKO Purkinje cells and enriched in AP-2α pull-down from WT cerebellum.

(C) Representative confocal image of Purkinje cells immunostained for AP-2α, GRID2IP, and calbindin. Scale bars: 20 μm; inset, 5 μm.

(D) Pearson's coefficient analysis of AP-2α and GRID2IP colocalization in dendrites of 2-month-old WT Purkinje cells ($N = 3$).

(E) Co-immunoprecipitation of AP-2α with GRID2IP in 2-month-old WT cerebellar lysates ($N = 3$). Input: 1.5% of the lysate.

(F and G) Immunoblot (F) and quantitative analysis (G) of GRID2IP levels in 2-month-old WT and cKO cerebella. Each dot represents one mouse ($N = 3$ per genotype). Statistical significance was determined by one-tailed unpaired Student's t test ($p = 0.0011$).

(H) Representative confocal images of WT and AP-2 cKO Purkinje cells immunostained for calbindin and GRID2IP. Scale bar: 20 μm.

(I) 3D analysis of GRID2IP distribution in 6-week-old AAV1/2-Ef1α-DIO-EYFP-transduced WT and AP-2 cKO Purkinje cells. Scale bars: 50 μm; inset, 10 μm.

(J) Quantification of GRID2IP voxels in Purkinje cell WT and AP-2 cKO dendrites. Each dot represents one cell (WT: $n = 17$ cells from $N = 3$ mice; cKO: $n = 9$ cells from $N = 3$ mice). Statistical significance was determined by unpaired two-tailed Student's t test ($p = 0.0043$).

(K and L) Multiplex fluorescence *in situ* hybridization for *Grid2ip* mRNA in 6-week-old AAV1/2-Ef1α-DIO-EYFP-transduced WT and cKO Purkinje cells (K) and quantitative analysis of *Grid2ip* mRNA puncta (L). Scale bars: 50 μm; inset, 20 μm. Each dot represents one mouse with $N = 3$ per genotype. Statistical significance was determined by unpaired two-tailed Student's t test ($p = 0.514$).

(M and N) Representative confocal images of DMSO- and/or MG132-treated (100 μM) acute cerebellar slices from 2-month-old WT and AP-2 cKO mice, immunostained for calbindin and GRID2IP (M), and quantification of GRID2IP protein levels (N). Each dot represents one cell (WT DMSO: $n = 233$ cells from $N = 4$ mice; WT MG132: $n = 253$ cells from $N = 4$ mice; cKO DMSO: $n = 233$ cells from $N = 4$ mice; cKO MG132: $n = 249$ cells from $N = 4$ mice). Statistical significance was determined by two-way ANOVA followed by Tukey's multiple-comparison test (all $p < 0.0001$). Scale bars: 50 μm; insets, 10 μm.

Data are presented as mean ± SEM. $^{*}p \leq 0.05$, $^{**}p \leq 0.01$, $^{***}p \leq 0.001$, $^{****}p \leq 0.0001$.

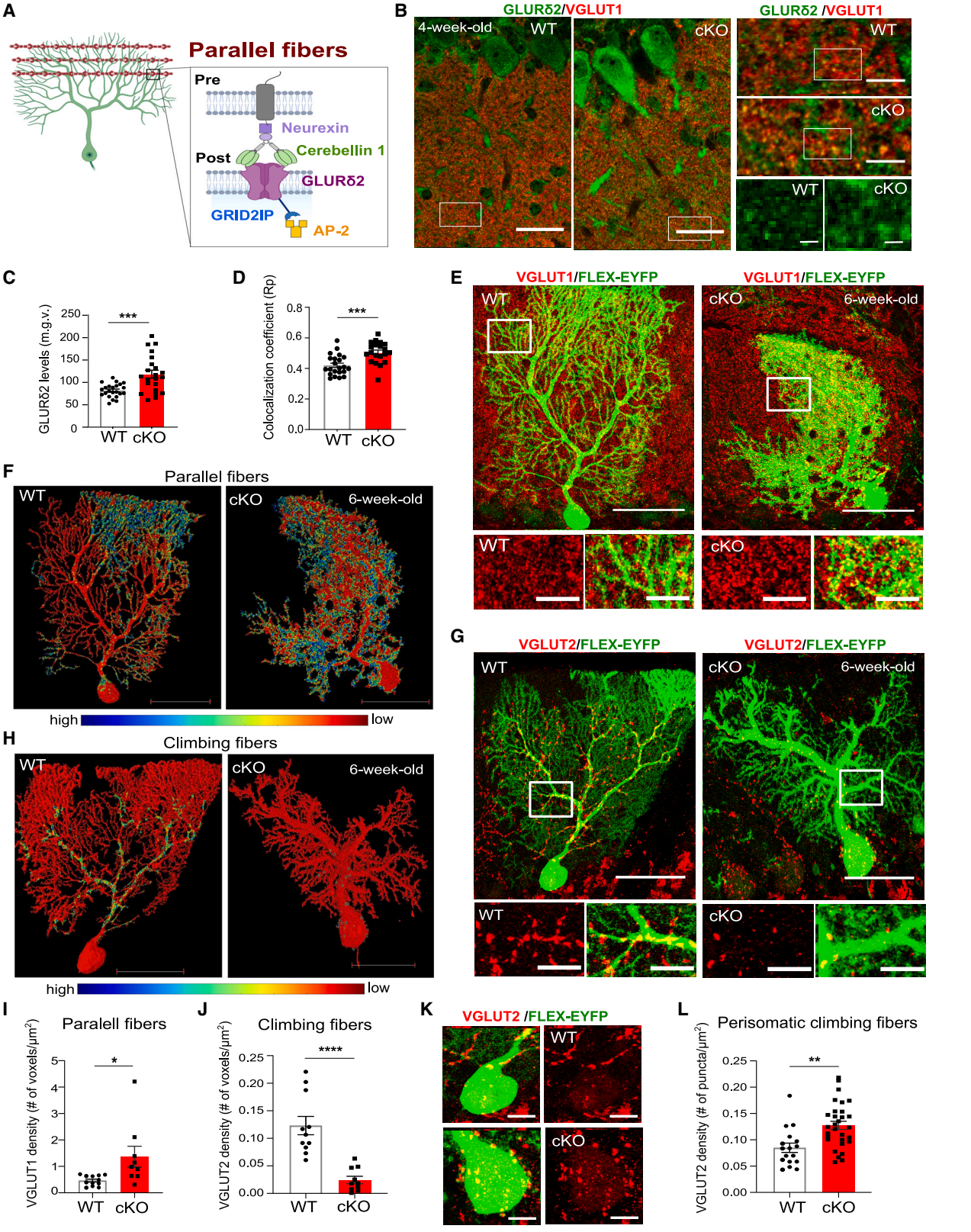

(legend on next page)

with the role of CF synapses in inhibiting neighboring Purkinje cells via ephaptic coupling.[71]

DISCUSSION

Using a Purkinje cell-specific AP-2 cKO mouse model, we demonstrate that AP-2 maintains the balance between PF and CF synapses. AP-2 loss results in Purkinje cell degeneration and severe motor deficits, driven partly by disrupted network activity due to unbalanced PF-CF input. Known for its role in CME,[72] AP-2 regulates synaptic vesicle recycling and neurotransmitter receptor trafficking.[26,27] While previous studies have examined its function in dendritogenesis and cargo sorting,[35,73–75] its role in neuronal circuitry formation has remained largely unexplored. Our study represents the first elucidation of AP-2 importance in orchestrating synaptic connectivity, suggesting its previously unrecognized role in shaping neuronal circuits.

While reduced dendritic complexity aligns with previous findings in cortical and hippocampal neurons,[35,74] the mature dendritic trees and increased spinogenesis of AP-2 cKO Purkinje cells imply that AP-2 does not directly control cerebellar dendrite morphology. Instead, AP-2 likely regulates synapse formation during early Purkinje cell maturation. This role may be specific to the cerebellum, where synaptic connectivity is refined postnatally.[76] Mechanistically, AP-2 interacts with GRID2IP, a postsynaptic scaffold enriched at PF synapses, where it links GLURδ2, a key regulator of PF synaptogenesis,[20,53,54,58] to the actin cytoskeleton. Mutations in GLURδ2 are associated with cerebellar ataxia in humans[57,77] and mice,[78,79] and GLURδ2 KO mice exhibit CF and PF misrouting.[20,56,58] Our data indicate that AP-2 prevents GRID2IP proteasomal degradation, with its loss leading to GLURδ2 accumulation at PF synapses, promoting their synaptogenesis. While many ionotropic glutamate receptors are found mainly intracellularly,[80] GLURδ2 predominantly resides on the plasma membrane,[81] suggesting that AP-2-mediated GRID2IP localization might be crucial for GLURδ2 endocytosis. GRID2IP-anchored actin filaments may facilitate dynamin-mediated membrane fission for GLURδ2 internalization, consistent with the role of other FH-domain proteins like mDia1 in regulating actin dynamics during endocytosis.[82]

A key finding of this study is the early onset of ataxia in AP-2 cKO mice, correlating with Purkinje cell degeneration by 2 months. This coincides with aberrant synaptic rewiring, including increased PF synapses and decreased CF inputs, which emerge as early as 4 weeks. The causal relationship between these events remains unclear. One hypothesis is that elevated PF synaptogenesis contributes to Purkinje cell degeneration through glutamate excitotoxicity, as observed in SCA models.[83,84] However, this hypothesis is speculative, as synaptic alterations and elevated Purkinje cell output appear at 4 weeks, while gait dysfunction and cell loss manifest 4 weeks later. Since granule cells proliferate exponentially in the first three postnatal weeks,[76] a fully developed PF network may be necessary for excitotoxicity to occur, possibly explaining the delay in Purkinje cell loss. Nonetheless, while increased Purkinje cell output and synaptic rewiring likely contribute to neurodegeneration, they are only part of a broader set of mechanisms driving this pathology.

Our data support the hypothesis that AP-2 balances cerebellar PF and CF synapses. First, AP-2 cKO cerebella show increased PF innervation and GLURδ2 enrichment at PF synapses by 4 weeks, followed by increased spinogenesis in Purkinje cells by 6 weeks. Second, somatic CF synapses are abundant in 4-week-old AP-2 cKO Purkinje cells but fail to translocate along Purkinje cell dendrites thereafter, indicating that the loss of CF innervation stems from Purkinje cell dysfunction, as AP-2 deletion is restricted to Purkinje cells. Third, increased Purkinje cell output, observed in 8-day-old Purkinje cells cultured *ex vivo* for 3 weeks, is rescued by ceftriaxone. Given that Bergmann glia density is unaltered in the AP-2 cKO cerebellum, the network effects are likely glia independent. Despite increased network output, Purkinje cell-intrinsic excitability is reduced, possibly due to downregulation of

Figure 5. Reorganization of PF and CF inputs in AP-2 cKO cerebellum

(A) Schematic of GLURδ2, GRID2IP, and AP-2 interaction at Purkinje cell-PF synapses.

(B) Representative confocal images of WT and AP-2 cKO cerebella immunostained for VGLUT1 and GLURδ2. Scale bars: 50 μm; insets, 10 μm (top) and 2 μm (bottom).

(C) GLURδ2 protein levels in distal Purkinje cell dendrites ($p = 0.0002$). Each dot represents one image (WT: $n = 23$ images from $N = 3$ mice, cKO $n = 22$ images from $N = 3$ mice).

(D) Pearson's correlation analysis of GLURδ2 and VGLUT1 colocalization at PF synapses in WT and AP-2 cKO Purkinje cells ($p = 0.0003$). Each dot represents one image (WT: $n = 22$ images from $N = 3$ mice, cKO: $n = 20$ images from $N = 3$ mice).

(E) Representative confocal images of AAV1/2-Ef1α-DIO-EYFP-transduced 6-week-old WT and AP-2 cKO Purkinje cells, immunostained for VGLUT1. Scale bar: 50 μm; insets, 10 μm.

(F) 3D analysis of VGLUT1 distribution in 6-week-old AAV1/2-Ef1α-DIO-EYFP-transduced WT and AP-2 cKO Purkinje cells. Scale bar: 50 μm.

(G) Representative confocal images of AAV1/2-Ef1α-DIO-EYFP-transduced 6-week-old WT and AP-2 cKO Purkinje cells, immunostained for VGLUT2. Scale bars: 50 μm; insets, 10 μm.

(H) 3D analysis of VGLUT2 distribution in 6-week-old AAV1/2-Ef1α-DIO-EYFP-transduced WT and AP-2 cKO Purkinje cells. Scale bar: 50 μm.

(I) Quantification of VGLUT1 punctum density in WT and AP-2 cKO Purkinje cells ($p = 0.017$). Each dot represents one cell (WT: $n = 11$ cells from $N = 4$ mice; cKO: $n = 9$ cells from $N = 3$ mice).

(J) Quantification of VGLUT2 punctum density in WT and AP-2 cKO Purkinje cells ($p < 0.0001$). Each dot represents one cell (WT: $n = 11$ cells from $N = 3$ mice; cKO: $n = 10$ cells from $N = 3$ mice).

(K) Magnified view of WT and AP-2 cKO Purkinje cell bodies from (G). Scale bar: 5 μm.

(L) Quantification of perisomatic VGLUT2 puncta in 6-week-old in WT and AP-2 cKO Purkinje cells ($p = 0.0012$). Each dot represents one cell (WT: $n = 17$ cells from $N = 3$ mice; cKO: $n = 30$ cells from $N = 3$ mice).

Data are presented as mean ± SEM. Statistical significance in (C), (D), (I) , (J), and (L) was determined by unpaired two-tailed Student's t test. $^{*}p \leq 0.05$, $^{**}p \leq 0.01$, $^{***}p \leq 0.001$, $^{****}p \leq 0.0001$.

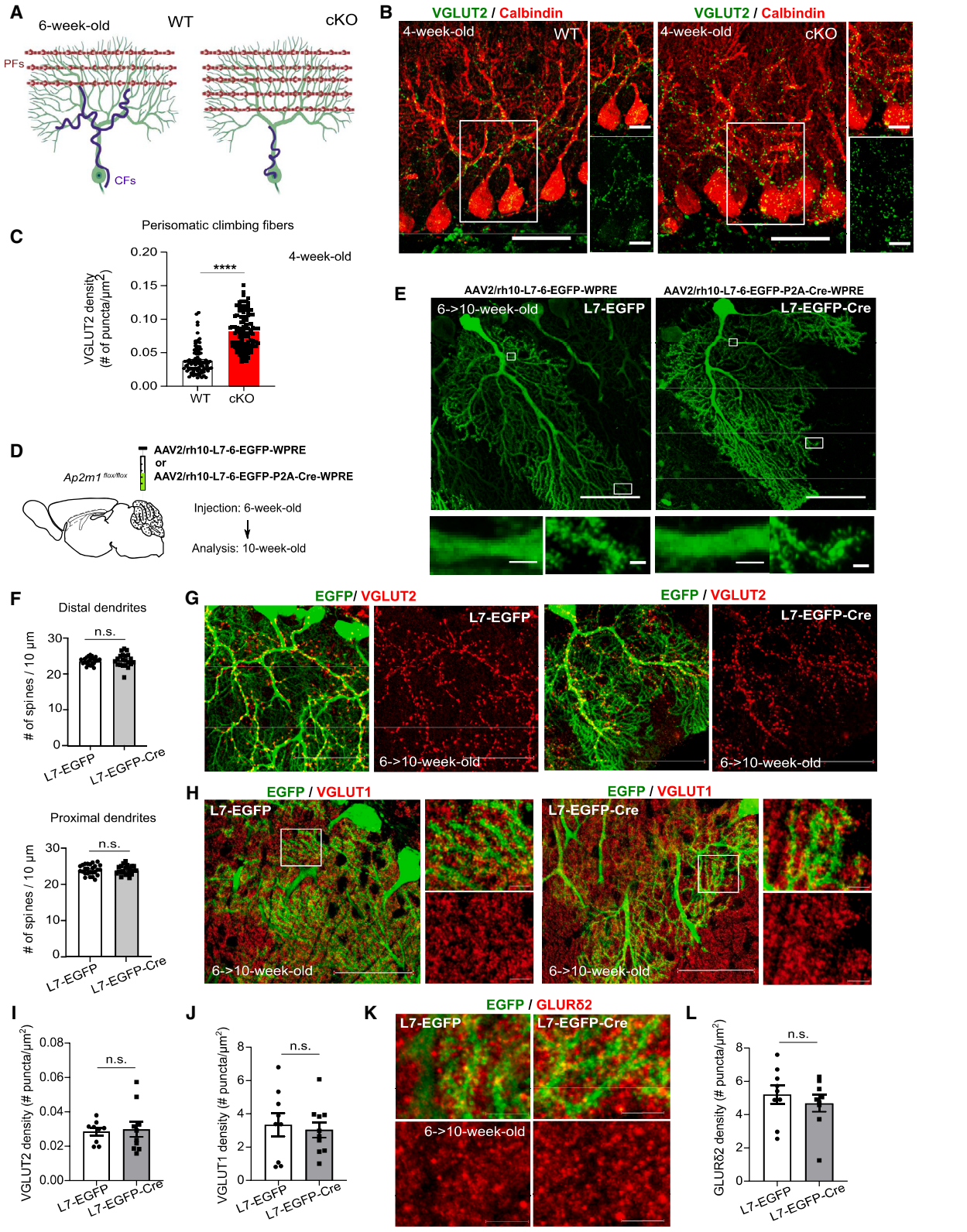

(legend on next page)

Ca^{2+}/calmodulin-dependent protein kinase II (CaMKII) subunits (Figure 3K and Tables S2 and S3), which modulate voltage-gated sodium channels,[85–87] and inhibition of CaMKII reduces Purkinje cell excitability.[88]

Our data align with the hypothesis that the increased network output due to an excess of PF synapses contributes to decreased CF innervation in mature Purkinje cells. Perturbed activity in Purkinje cells can affect CF translocation,[89] as observed in *weaver*,[90] *staggerer*,[91] and *reeler*[92] mice, where granule cells (the source of PFs) degenerate or are absent. Our data further indicate that deleting AP-2 after post-natal day 21, when the CF territory is already fully established, does not impact CF translocation. Given the essential role of CFs in cerebellar learning and motor function[3] and the severe motor deficits caused by genetic silencing of olivocerebellar synapses,[93] we propose that impaired CF innervation drives motor deficits in AP-2 cKO mice, although further experiments are needed to confirm this.

Our findings suggest that increased PF synaptogenesis enhances Purkinje cell network output, blocking CF translocation in AP-2 cKO mice. However, excess PF inputs can also provide trophic support and inhibit CF translocation. Alterations in brain-derived neurotrophic factor (BDNF) and its receptor, TrkB, have been implicated in SCA6,[23,94] with TrkB inactivation shown to slow CF elimination.[95] Overactivation of α-amino-3-hydroxy-5-methyl-4-isoxazolepropionic acid (AMPA)-mediated synaptic transmission at PF-Purkinje cell synapses may also impair mitochondrion function and induce reactive oxygen species (ROS) formation, negatively affecting synapse density.[96] AP-2 may also regulate synaptic plasticity by controlling AMPA receptor trafficking. Components of CME are known to regulate cerebellar long-term depression (LTD),[97] and AP-2α is crucial for LTD-driven AMPA receptor endocytosis.[98] While LTD is essential for synaptic plasticity, its slow timescale does not fully account for the rapid changes in Purkinje cell output captured by the Ca^{2+} imaging approach in the current study.[64] Last, despite the association between GRIDIP levels and PF/CF imbalance reported here, GRID2IP KO mice show no phenotype.[99] We hypothesize that this discrepancy is due to the differential timing of GRID2IP deletion so that compensatory mechanisms may localize GLURδ2 in the absence of GRID2IP in the embryonic deletion model (e.g., through upregulation of PSD-93[100]).

In summary, our study reveals the critical role of AP-2 in cerebellar synaptogenesis and motor coordination with implications for ataxia and cerebellar disorders. Our observations are relevant to a recently described mutation in *AP2M1* associated with developmental encephalopathy accompanied by ataxia.[29] We propose that ataxic symptoms in these patients may result from disrupted cerebellar synaptogenesis due to AP-2 loss of function.

Limitations of the study

Our findings have several limitations. The molecular interaction between AP-2 and GRID2IP at PF synapses remains incompletely resolved. While we propose a model involving AP-2-mediated stabilization of GRID2IP to regulate GLURδ2 endocytosis, direct evidence of this pathway is lacking. The link between synaptic rewiring, increased Purkinje cell activity, and degeneration remains speculative and requires longitudinal *in vivo* imaging and behavioral studies to further clarify this aspect. The role of compensatory endocytic adaptors or changes in the plasma membrane proteome also remains unexplored. Proteomic analyses of plasma membrane proteins in AP-2-deficient Purkinje cells may reveal additional pathways contributing to the observed phenotypes. Future studies addressing these gaps will enhance our understanding of the role of AP-2 in cerebellar function and its therapeutic potential.

RESOURCE AVAILABILITY

Lead contact

Requests for further information, resources, or reagents should be directed to the lead contact, Natalia Kononenko (n.kononenko@uni-koeln.de).

Materials availability

AAV2/rh10-L7-6-EGFP-WPRE and AAV2/rh10-L7-6-EGFP-P2A-Cre-WPRE will be deposited in Addgene upon publication (https://www.addgene.org/Günter_Schwarz/).

Data and code availability

- The proteomics data have been deposited at ProteomeXchange via the PRIDE partner repository and are publicly available as of the date of publication. Accession numbers are listed in the key resources table. Microscopy data reported in this paper will be shared by the lead contact upon request.
- This paper does not report original code.

Figure 6. Acute AP-2μ deletion in the adult cerebellum does not induce CF rewiring

(A) Schematic of PF-CF synapse reorganization in AP-2 cKO cerebellum. Created in BioRender.

(B and C) Representative confocal images of WT and AP-2 cKO cerebella, immunostained for VGLUT2 and Calbindin (B), and quantitative analysis of perisomatic VGLUT2 puncta (C). Scale bars: 50 μm; insets, 10 μm. Each dot represents one cell (WT: $n = 92$ cells from $N = 3$ mice; cKO: $n = 104$ cells from $N = 3$ mice) ($p < 0.0001$).

(D) AAV2/rh10-L7-6-EGFP-P2A-Cre-WPRE (L7-EGFP-Cre) injection timeline. L7-EGFP was used as a control.

(E) Representative confocal images of 10-week-old Purkinje cells transduced with either L7-EGFP-Cre or L7-EGFP. Scale bars: 50 μm; insets, 10 and 2 μm.

(F) Spine count in Purkinje cells with acute AP-2μ deletion. Each dot represents one cell (proximal dendrites: L7-EGFP: 24 cells from $N = 3$ mice; L7-EGFP-Cre: $n = 21$ cells from $N = 3$ mice. Distal dendrites: L7-EGFP: 26 cells from $N = 3$ mice; L7-EGFP-Cre: $n = 21$ cells from $N = 3$ mice).

(G and H) Representative confocal images of 10-week-old Purkinje cells transduced with either L7-EGFP-Cre or L7-EGFP, immunostained for VGLUT2 (G) and/or VLGUT1 (H). Scale bars: 50 μm; insets in (H), 10 μm.

(I and J) VGLUT2 (I) and VGLUT1 (J) punctum density in Purkinje cells with AP-2μ acute deletion. $N = 9$ images from L7-EGFP and $n = 10$ images from L7-EGFP-Cre-injected mice (each with >5 cells); $N = 3$ mice for each condition.

(K and L) Representative confocal images of 10-week-old Purkinje cells transduced with either L7-EGFP-Cre or L7-EGFP, immunostained for GLURδ2 (K), and quantitative analysis (L). Scale bar: 5 μm. Each dot represents one image (with >5 cells) with $n = 9$ images from $N = 3$ mice for each condition.

Data are presented as mean ± SEM. Statistical significance in (C), (F), (I), (J), and (L) was determined by unpaired two-tailed Student's t test. $^{*}p \leq 0.05$, $^{**}p \leq 0.01$, $^{***}p \leq 0.001$, $^{****}p \leq 0.0001$.

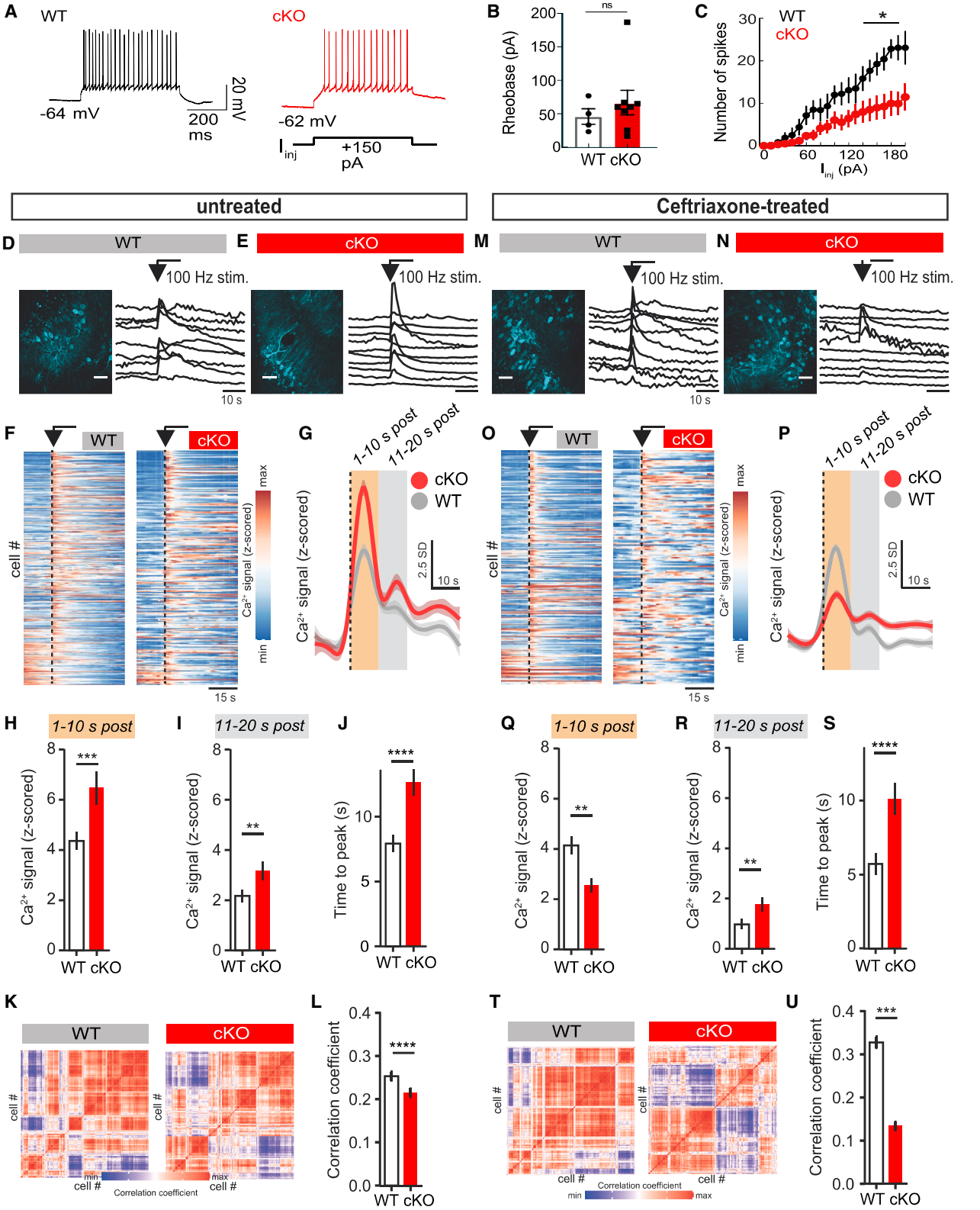

(legend on next page)

- Any additional information required to reanalyze the data reported in this paper is available from the lead contact upon request.

ACKNOWLEDGMENTS

We thank R. Renn and Dr. M. Schröter for their expert assistance. We are indebted to Dr. C. Jüngst (CECAD Imaging Facility) and Dr. S. Müller and Dr. J.-W. Lackmann (CECAD Proteomic Facility) for their help and expert assistance. We thank Prof. E. Rugarli (CECAD, University of Cologne) for providing L7-Cre transgenic mice. The work of N.L.K. is funded by the Deutsche Forschungsgemeinschaft (DFG, German Research Foundation): EXC 2030–390661388, KO 5091/4-1, DFG-431549029-SFB 1451, DFG-233886668-GRK1960 and DFG-411422114-GRK 2550. I.K. and QS are funded by the Nordrhein-Westfalen (NRW) network iBehave.

AUTHOR CONTRIBUTIONS

Conceptualization, N.L.K. and M.T.; methodology, M.T., J.T., F.L., A.P., S.V., G.G., and N.L.K.; investigation, M.T., J.T., E.Ö.-Y., V.J.F., M.O., I.K., E.K., Q.S., S.V., G.G., and N.L.K.; visualization, M.T., J.T., I.K., A.P., S.V., G.G., and N.L.K.; supervision, T.K., G.S., S.V., G.G., and N.L.K.; writing – original draft, M.T. and N.L.K.; writing – review & editing, N.L.K.

DECLARATION OF INTERESTS

The authors declare no competing interests.

STAR★METHODS

Detailed methods are provided in the online version of this paper and include the following:

SUPPLEMENTAL INFORMATION

Supplemental information can be found online at https://doi.org/10.1016/j.celrep.2025.115256.

Figure 7. AP-2 functions in Purkinje cells to regulate cerebellar network excitability

(A) Example whole-cell recordings of WT and AP-2 cKO Purkinje cells in 4-week-old acute cerebellar slices in response to 150 pA intracellular current injection.
(B and C) Analysis of Purkinje cell rheobase (B) and spike number (C) (WT $n = 4$ cells from $N = 3$ mice, cKO $n = 8$ cells from $N = 2$ mice). Statistical significance was determined by two-tailed Mann-Whitney test.
(D and E) Representative responses to 100 Hz stimulation for 1 s in WT (D) and AP-2 cKO (E) Purkinje cells transduced with ssAAV-9/2-mCaMKIIα-jGCaMP7f-WPRE-bGHp(A). Each trace represents one cell. Scale bar, 50 μm.
(F) Activity map across all neurons sorted by maximum response to stimulation.
(G–I) Peri-stimulus response (G) and quantification of response during either 1–10 s (H) or 11–20 s (I) post stimulation in WT or AP-2 cKO Purkinje cells (H: $p = 0.0002$; I: $p = 0.001$). Data are from $N = 6$ WT and $N = 5$ cKO mice with 457 and 255 Purkinje cells, respectively.
(J) Time to reach maximal Ca^{2+} response following 100 Hz stimulation in WT and AP-2 cKO Purkinje cells transduced with ssAAV-9/2-mCaMKIIα-jGCaMP7f-WPRE-bGHp(A) ($p < 0.0001$). Data are from $N = 6$ WT and $N = 5$ cKO mice with 445 and 251 Purkinje cells, respectively.
(K and L) Correlation matrix (K) and quantification (L) of stimulus-evoked responses across all WT (left) and AP-2 cKO Purkinje cells (right) ($p < 0.0001$). Data are from $N = 6$ WT and $N = 5$ cKO mice with 457 and 255 Purkinje cells, respectively.
(M and N) Representative responses to 100 Hz stimulation in WT (M) and AP-2 cKO (N) Purkinje cells transduced with AAV-CamKIIα-GCaMP7f and treated with 100 μM ceftriaxone for 7 days. Each trace represents one cell. Scale bar, 50 μm.
(O) Activity map across all neurons treated with 100 μM ceftriaxone, sorted by maximum response to stimulation.
(P–R) Peri-stimulus response (P) and quantification of response during either 1–10 s (Q) or 11–20 s (R) post stimulation in Purkinje cells from WT or AP-2 cKO cerebellar organotypic slices treated with 100 μM ceftriaxone (Q: $p = 0.001$, R: $p = 0.002$). Data are from $N = 4$ WT and $N = 2$ cKO mice with 277 and 164 Purkinje cells, respectively.
(S) Time to reach maximal Ca^{2+} response following 100 Hz stimulation in WT and AP-2 cKO Purkinje cells transduced with ssAAV-9/2-mCaMKIIα-jGCaMP7f-WPRE-bGHp(A) and treated with 100 μM ceftriaxone ($p < 0.0001$). Data are from $N = 4$ WT and $N = 2$ cKO mice with 262 and 155 Purkinje cells, respectively.
(T and U) Correlation matrix (T) and quantification (U) of stimulus-evoked responses in WT (left) and AP-2 cKO cells (right) after ceftriaxone treatment ($p < 0.0001$). Data are from $N = 4$ WT and $N = 2$ cKO mice with 277 and 164 Purkinje cells, respectively.
Data are presented as mean ± SEM. Statistical significance in (H)–(J), (L), (Q)–(S), and (U) was determined by Welch's t test. $^{*}p \leq 0.05$, $^{**}p \leq 0.01$, $^{***}p \leq 0.001$, $^{****}p \leq 0.0001$.

Received: June 11, 2024
Revised: December 2, 2024
Accepted: January 10, 2025
Published: February 6, 2025

REFERENCES

1. Carey, M.R. (2024). The cerebellum. Curr. Biol. *34*, R7–R11. https://doi.org/10.1016/j.cub.2023.11.048.
2. Yang, Y., and Lisberger, S.G. (2014). Purkinje-cell plasticity and cerebellar motor learning are graded by complex-spike duration. Nature *510*, 529–532. https://doi.org/10.1038/nature13282.
3. Silva, N.T., Ramírez-Buriticá, J., Pritchett, D.L., and Carey, M.R. (2024). Climbing fibers provide essential instructive signals for associative learning. Nat. Neurosci. *27*, 940–951. https://doi.org/10.1038/s41593-024-01594-7.
4. Carey, M.R. (2011). Synaptic mechanisms of sensorimotor learning in the cerebellum. Curr. Opin. Neurobiol. *21*, 609–615. https://doi.org/10.1016/j.conb.2011.06.011.
5. Smeets, C.J.L.M., and Verbeek, D.S. (2016). Climbing fibers in spinocerebellar ataxia: A mechanism for the loss of motor control. Neurobiol. Dis. *88*, 96–106. https://doi.org/10.1016/j.nbd.2016.01.009.
6. Ebner, B.A., Ingram, M.A., Barnes, J.A., Duvick, L.A., Frisch, J.L., Clark, H.B., Zoghbi, H.Y., Ebner, T.J., and Orr, H.T. (2013). Purkinje Cell Ataxin-1 Modulates Climbing Fiber Synaptic Input in Developing and Adult Mouse Cerebellum. J. Neurosci. *33*, 5806–5820. https://doi.org/10.1523/JNEUROSCI.6311-11.2013.
7. Barnes, J.A., Ebner, B.A., Duvick, L.A., Gao, W., Chen, G., Orr, H.T., and Ebner, T.J. (2011). Abnormalities in the climbing fiber-Purkinje cell circuitry contribute to neuronal dysfunction in ATXN1[82Q] mice. J. Neurosci. *31*, 12778–12789. https://doi.org/10.1523/jneurosci.2579-11.2011.
8. Furrer, S.A., Waldherr, S.M., Mohanachandran, M.S., Baughn, T.D., Nguyen, K.-T., Sopher, B.L., Damian, V.A., Garden, G.A., and La Spada, A.R. (2013). Reduction of mutant ataxin-7 expression restores motor function and prevents cerebellar synaptic reorganization in a conditional mouse model of SCA7. Hum. Mol. Genet. *22*, 890–903. https://doi.org/10.1093/hmg/dds495.
9. Shuvaev, A.N., Horiuchi, H., Seki, T., Goenawan, H., Irie, T., Iizuka, A., Sakai, N., and Hirai, H. (2011). Mutant PKCγ in Spinocerebellar Ataxia Type 14 Disrupts Synapse Elimination and Long-Term Depression in Purkinje Cells in vivo. J. Neurosci. *31*, 14324–14334. https://doi.org/10.1523/JNEUROSCI.5530-10.2011.
10. Smeets, C.J.L.M., Jezierska, J., Watanabe, H., Duarri, A., Fokkens, M.R., Meijer, M., Zhou, Q., Yakovleva, T., Boddeke, E., den Dunnen, W., et al. (2015). Elevated mutant dynorphin A causes Purkinje cell loss and motor dysfunction in spinocerebellar ataxia type 23. Brain *138*, 2537–2552. https://doi.org/10.1093/brain/awv195.
11. Smeets, C.J.L.M., Ma, K.Y., Fisher, S.E., and Verbeek, D.S. (2021). Cerebellar developmental deficits underlie neurodegenerative disorder spinocerebellar ataxia type 23. Brain Pathol. *31*, 239–252. https://doi.org/10.1111/bpa.12905.
12. Hashimoto, K., and Kano, M. (2013). Synapse elimination in the developing cerebellum. Cell. Mol. Life Sci. *70*, 4667–4680. https://doi.org/10.1007/s00018-013-1405-2.
13. Sotelo, C., Hillman, D.E., Zamora, A.J., and Llinás, R. (1975). Climbing fiber deafferentation: Its action on Purkinje cell dendritic spines. Brain Res. *98*, 574–581. https://doi.org/10.1016/0006-8993(75)90374-1.
14. Miyazaki, T., Hashimoto, K., Shin, H.-S., Kano, M., and Watanabe, M. (2004). P/Q-Type Ca2+ Channel α1A Regulates Synaptic Competition on Developing Cerebellar Purkinje Cells. J. Neurosci. *24*, 1734–1743. https://doi.org/10.1523/JNEUROSCI.4208-03.2004.
15. Miyazaki, T., Yamasaki, M., Takeuchi, T., Sakimura, K., Mishina, M., and Watanabe, M. (2010). Ablation of glutamate receptor GluRδ2 in adult Purkinje cells causes multiple innervation of climbing fibers by inducing aberrant invasion to parallel fiber innervation territory. J. Neurosci. *30*, 15196–15209. https://doi.org/10.1523/jneurosci.0934-10.2010.
16. Miyazaki, T., Yamasaki, M., Hashimoto, K., Yamazaki, M., Abe, M., Usui, H., Kano, M., Sakimura, K., and Watanabe, M. (2012). Cav2.1 in cerebellar Purkinje cells regulates competitive excitatory synaptic wiring, cell survival, and cerebellar biochemical compartmentalization. J. Neurosci. *32*, 1311–1328. https://doi.org/10.1523/jneurosci.2755-11.2012.
17. Ohtsuki, G., Piochon, C., and Hansel, C. (2009). Climbing fiber signaling and cerebellar gain control. Front. Cell. Neurosci. *3*, 4. https://doi.org/10.3389/neuro.03.004.2009.
18. Kakizawa, S., Yamada, K., Iino, M., Watanabe, M., and Kano, M. (2003). Effects of insulin-like growth factor I on climbing fibre synapse elimination during cerebellar development. Eur. J. Neurosci. *17*, 545–554. https://doi.org/10.1046/j.1460-9568.2003.02486.x.
19. Bosman, L.W.J., Hartmann, J., Barski, J.J., Lepier, A., Noll-Hussong, M., Reichardt, L.F., and Konnerth, A. (2006). Requirement of TrkB for synapse elimination in developing cerebellar Purkinje cells. Brain Cell Biol. *35*, 87–101. https://doi.org/10.1007/s11068-006-9002-z.
20. Ichikawa, R., Miyazaki, T., Kano, M., Hashikawa, T., Tatsumi, H., Sakimura, K., Mishina, M., Inoue, Y., and Watanabe, M. (2002). Distal extension of climbing fiber territory and multiple innervation caused by aberrant wiring to adjacent spiny branchlets in cerebellar Purkinje cells lacking glutamate receptor delta 2. J. Neurosci. *22*, 8487–8503. https://doi.org/10.1523/jneurosci.22-19-08487.2002.
21. Hashimoto, K., Tsujita, M., Miyazaki, T., Kitamura, K., Yamazaki, M., Shin, H.-S., Watanabe, M., Sakimura, K., and Kano, M. (2011). Postsynaptic P/Q-type Ca2+ channel in Purkinje cell mediates synaptic competition and elimination in developing cerebellum. Proc. Natl. Acad. Sci. USA *108*, 9987–9992. https://doi.org/10.1073/pnas.1101488108.
22. Kano, M., Hashimoto, K., Kurihara, H., Watanabe, M., Inoue, Y., Aiba, A., and Tonegawa, S. (1997). Persistent multiple climbing fiber innervation of cerebellar Purkinje cells in mice lacking mGluR1. Neuron *18*, 71–79. https://doi.org/10.1016/s0896-6273(01)80047-7.
23. Cook, A.A., Jayabal, S., Sheng, J., Fields, E., Leung, T.C.S., Quilez, S., McNicholas, E., Lau, L., Huang, S., and Watt, A.J. (2022). Activation of TrkB-Akt signaling rescues deficits in a mouse model of SCA6. Sci. Adv. *8*, eabh3260. https://doi.org/10.1126/sciadv.abh3260.
24. Zhang, B., Chen, L.Y., Liu, X., Maxeiner, S., Lee, S.J., Gokce, O., and Südhof, T.C. (2015). Neuroligins Sculpt Cerebellar Purkinje-Cell Circuits by Differential Control of Distinct Classes of Synapses. Neuron *87*, 781–796. https://doi.org/10.1016/j.neuron.2015.07.020.
25. Robinson, M.S. (2004). Adaptable adaptors for coated vesicles. Trends Cell Biol. *14*, 167–174. https://doi.org/10.1016/j.tcb.2004.02.002.
26. Camblor-Perujo, S., and Kononenko, N.L. (2022). Brain-specific functions of the endocytic machinery. FEBS J. *289*, 2219–2246. https://doi.org/10.1111/febs.15897.
27. Kononenko, N.L., and Haucke, V. (2015). Molecular Mechanisms of Presynaptic Membrane Retrieval and Synaptic Vesicle Reformation. Neuron *85*, 484–496. https://doi.org/10.1016/j.neuron.2014.12.016.
28. Dittman, J., and Ryan, T.A. (2009). Molecular circuitry of endocytosis at nerve terminals. Annu. Rev. Cell Dev. Biol. *25*, 133–160. https://doi.org/10.1146/annurev.cellbio.042308.113302.
29. Helbig, I., Lopez-Hernandez, T., Shor, O., Galer, P., Ganesan, S., Pendziwiat, M., Rademacher, A., Ellis, C.A., Hümpfer, N., Schwarz, N., et al. (2019). A Recurrent Missense Variant in AP2M1 Impairs Clathrin-Mediated Endocytosis and Causes Developmental and Epileptic Encephalopathy. Am. J. Hum. Genet. *104*, 1060–1072. https://doi.org/10.1016/j.ajhg.2019.04.001.
30. Gu, M., Schuske, K., Watanabe, S., Liu, Q., Baum, P., Garriga, G., and Jorgensen, E.M. (2008). Mu2 adaptin facilitates but is not essential for

synaptic vesicle recycling in Caenorhabditis elegans. J. Cell Biol. *183*, 881–892. https://doi.org/10.1083/jcb.200806088.

31. Gu, M., Liu, Q., Watanabe, S., Sun, L., Hollopeter, G., Grant, B.D., and Jorgensen, E.M. (2013). AP2 hemicomplexes contribute independently to synaptic vesicle endocytosis. Elife *2*, e00190. https://doi.org/10.7554/eLife.00190.
32. Kim, S.H., and Ryan, T.A. (2009). Synaptic vesicle recycling at CNS snapses without AP-2. J. Neurosci. *29*, 3865–3874. https://doi.org/10.1523/JNEUROSCI.5639-08.2009.
33. Kononenko, N.L., Puchkov, D., Classen, G.A., Walter, A.M., Pechstein, A., Sawade, L., Kaempf, N., Trimbuch, T., Lorenz, D., Rosenmund, C., et al. (2014). Clathrin/AP-2 Mediate Synaptic Vesicle Reformation from Endosome-like Vacuoles but Are Not Essential for Membrane Retrieval at Central Synapses. Neuron *82*, 981–988. https://doi.org/10.1016/j.neuron.2014.05.007.
34. Bera, S., Camblor-Perujo, S., Calleja Barca, E., Negrete-Hurtado, A., Racho, J., De Bruyckere, E., Wittich, C., Ellrich, N., Martins, S., Adjaye, J., and Kononenko, N.L. (2020). AP2 reduces amyloidogenesis by promoting BACE 1 trafficking and degradation in neurons. EMBO reports *Jun 4 21*, e47954. https://doi.org/10.15252/embr.201947954.
35. Kononenko, N.L., Claßen, G.A., Kuijpers, M., Puchkov, D., Maritzen, T., Tempes, A., Malik, A.R., Skalecka, A., Bera, S., Jaworski, J., and Haucke, V. (2017). Retrograde transport of TrkB-containing autophagosomes via the adaptor AP-2 mediates neuronal complexity and prevents neurodegeneration. Nat. Commun. *8*, 1–16. https://doi.org/10.1038/ncomms14819. http://www.nature.com/articles/ncomms14819#supplementary-information.
36. Andres-Alonso, M., Ammar, M.R., Butnaru, I., Gomes, G.M., Acuña Sanhueza, G., Raman, R., Yuanxiang, P., Borgmeyer, M., Lopez-Rojas, J., Raza, S.A., et al. (2019). SIPA1L2 controls trafficking and local signaling of TrkB-containing amphisomes at presynaptic terminals. Nat. Commun. *10*, 5448. https://doi.org/10.1038/s41467-019-13224-z.
37. Camblor-Perujo, S., Ozer Yildiz, E., Küpper, H., Overhoff, M., Rastogi, S., Bazzi, H., and Kononenko, N.L. (2024). The AP-2 complex interacts with γ-TuRC and regulates the proliferative capacity of neural progenitors. Life Sci. Alliance *7*, e202302029. https://doi.org/10.26508/lsa.202302029.
38. Barski, J.J., Dethleffsen, K., and Meyer, M. (2000). Cre recombinase expression in cerebellar Purkinje cells. Genesis *28*, 93–98.
39. Kozareva, V., Martin, C., Osorno, T., Rudolph, S., Guo, C., Vanderburg, C., Nadaf, N., Regev, A., Regehr, W.G., and Macosko, E. (2021). A transcriptomic atlas of mouse cerebellar cortex comprehensively defines cell types. Nature *598*, 214–219. https://doi.org/10.1038/s41586-021-03220-z.
40. Sathyamurthy, A., Barik, A., Dobrott, C.I., Matson, K.J.E., Stoica, S., Pursley, R., Chesler, A.T., and Levine, A.J. (2020). Cerebellospinal Neurons Regulate Motor Performance and Motor Learning. Cell Rep. *31*, 107595. https://doi.org/10.1016/j.celrep.2020.107595.
41. Miterko, L.N., Lin, T., Zhou, J., van der Heijden, M.E., Beckinghausen, J., White, J.J., and Sillitoe, R.V. (2021). Neuromodulation of the cerebellum rescues movement in a mouse model of ataxia. Nat. Commun. *12*, 1295. https://doi.org/10.1038/s41467-021-21417-8.
42. Hosseini, M., Klein, I., Kuzu, T.D., Semmler, C., Wunderle, V., Mardare, V., Galvao, A., Haustein, M., Büschges, A., Grefkes, C., et al. (2024). AutoGaitA – Automated Gait Analysis in Python. bioRxiv. https://doi.org/10.1101/2024.04.14.589409.
43. Ilg, W., Golla, H., Thier, P., and Giese, M.A. (2007). Specific influences of cerebellar dysfunctions on gait. Brain *130*, 786–798. https://doi.org/10.1093/brain/awl376.
44. Ilg, W., and Timmann, D. (2013). Gait ataxia—specific cerebellar influences and their rehabilitation. Mov. Disord. *28*, 1566–1575. https://doi.org/10.1002/mds.25558.
45. Hannoun, S., and ani, R. (2022). Editorial: MRI-Based Methods for the Identification of Cerebellar Ataxia Types. Front. Neurosci. *16*, 847726. https://doi.org/10.3389/fnins.2022.847726.
46. Hoxha, E., Balbo, I., Miniaci, M.C., and Tempia, F. (2018). Purkinje Cell Signaling Deficits in Animal Models of Ataxia. Front. Synaptic Neurosci. *10*, 6. https://doi.org/10.3389/fnsyn.2018.00006.
47. López-Hernández, T., Takenaka, K.-i., Mori, Y., Kongpracha, P., Nagamori, S., Haucke, V., and Takamori, S. (2022). Clathrin-independent endocytic retrieval of SV proteins mediated by the clathrin adaptor AP-2 at mammalian central synapses. Elife *11*, e71198. https://doi.org/10.7554/eLife.71198.
48. Miyagi, Y., Yamashita, T., Fukaya, M., Sonoda, T., Okuno, T., Yamada, K., Watanabe, M., Nagashima, Y., Aoki, I., Okuda, K., et al. (2002). Delphilin: a Novel PDZ and Formin Homology Domain-Containing Protein that Synaptically Colocalizes and Interacts with Glutamate Receptor δ2 Subunit. J. Neurosci. *22*, 803–814. https://doi.org/10.1523/JNEUROSCI.22-03-00803.2002.
49. DeWard, A.D., and Alberts, A.S. (2009). Ubiquitin-mediated degradation of the formin mDia2 upon completion of cell division. J. Biol. Chem. *284*, 20061–20069. https://doi.org/10.1074/jbc.M109.000885.
50. Lomeli, H., Sprengel, R., Laurie, D.J., Köhr, G., Herb, A., Seeburg, P.H., and Wisden, W. (1993). The rat delta-1 and delta-2 subunits extend the excitatory amino acid receptor family. FEBS Lett. *315*, 318–322. https://doi.org/10.1016/0014-5793(93)81186-4.
51. Takayama, C., Nakagawa, S., Watanabe, M., Mishina, M., and Inoue, Y. (1995). Light- and electron-microscopic localization of the glutamate receptor channel 62 subunit in the mouse Purkinje cell. Neurosci. Lett. *188*, 89–92. https://doi.org/10.1016/0304-3940(95)11403-J.
52. Fremeau, R.T., Jr., Troyer, M.D., Pahner, I., Nygaard, G.O., Tran, C.H., Reimer, R.J., Bellocchio, E.E., Fortin, D., Storm-Mathisen, J., and Edwards, R.H. (2001). The expression of vesicular glutamate transporters defines two classes of excitatory synapse. Neuron *31*, 247–260. https://doi.org/10.1016/s0896-6273(01)00344-0.
53. Matsuda, K., Miura, E., Miyazaki, T., Kakegawa, W., Emi, K., Narumi, S., Fukazawa, Y., Ito-Ishida, A., Kondo, T., Shigemoto, R., et al. (2010). Cbln1 is a ligand for an orphan glutamate receptor delta2, a bidirectional synapse organizer. Science (New York, N.Y.) *328*, 363–368. https://doi.org/10.1126/science.1185152.
54. Uemura, T., Lee, S.-J., Yasumura, M., Takeuchi, T., Yoshida, T., Ra, M., Taguchi, R., Sakimura, K., and Mishina, M. (2010). Synaptic Interaction of GluRδ2 and Neurexin through Cbln1 Mediates Synapse Formation in the Cerebellum. Cell *141*, 1068–1079. https://doi.org/10.1016/j.cell.2010.04.035.
55. Yuzaki, M. (2017). The C1q complement family of synaptic organizers: not just complementary. Curr. Opin. Neurobiol. *45*, 9–15. https://doi.org/10.1016/j.conb.2017.02.002.
56. Kashiwabuchi, N., Ikeda, K., Araki, K., Hirano, T., Shibuki, K., Takayama, C., Inoue, Y., Kutsuwada, T., Yagi, T., Kang, Y., et al. (1995). Impairment of motor coordination, Purkinje cell synapse formation, and cerebellar long-term depression in GluRδ2 mutant mice. Cell *81*, 245–252. https://doi.org/10.1016/0092-8674(95)90334-8.
57. Panda, P.K., Sharawat, I.K., and Dawman, L. (2022). GRID2 Mutation-Related Spinocerebellar Ataxia Type 18: A New Report and Literature Review. J. Pediatr. Genet. *11*, 99–109. https://doi.org/10.1055/s-0040-1721084.
58. Kurihara, H., Hashimoto, K., Kano, M., Takayama, C., Sakimura, K., Mishina, M., Inoue, Y., and Watanabe, M. (1997). Impaired Parallel Fiber→Purkinje Cell Synapse Stabilization during Cerebellar Development of Mutant Mice Lacking the Glutamate Receptor δ2 Subunit. J. Neurosci. *17*, 9613–9623. https://doi.org/10.1523/JNEUROSCI.17-24-09613.1997.
59. Takeo, Y.H., Shuster, S.A., Jiang, L., Hu, M.C., Luginbuhl, D.J., Rülicke, T., Contreras, X., Hippenmeyer, S., Wagner, M.J., Ganguli, S., and Luo, L. (2021). GluD2- and Cbln1-mediated competitive interactions shape the dendritic arbors of cerebellar Purkinje cells. Neuron *109*, 629–644.e8. https://doi.org/10.1016/j.neuron.2020.11.028.
60. Busch, S.E., and Hansel, C. (2023). Climbing fiber multi-innervation of mouse Purkinje dendrites with arborization common to human. Science

(New York, N.Y.) *381*, 420–427. https://doi.org/10.1126/science.adi1024.

61. Carrillo, J., Nishiyama, N., and Nishiyama, H. (2013). Dendritic Translocation Establishes the Winner in Cerebellar Climbing Fiber Synapse Elimination. J. Neurosci. *33*, 7641–7653. https://doi.org/10.1523/JNEUROSCI.4561-12.2013.

62. Hashimoto, K., Ichikawa, R., Kitamura, K., Watanabe, M., and Kano, M. (2009). Translocation of a "Winner" Climbing Fiber to the Purkinje Cell Dendrite and Subsequent Elimination of "Losers" from the Soma in Developing Cerebellum. Neuron *63*, 106–118. https://doi.org/10.1016/j.neuron.2009.06.008.

63. Scelfo, B., Strata, P., and Knöpfel, T. (2003). Sodium imaging of climbing fiber innervation fields in developing mouse Purkinje cells. J. Neurophysiol. *89*, 2555–2563. https://doi.org/10.1152/jn.00884.2002.

64. Gilbert, P.F., and Thach, W.T. (1977). Purkinje cell activity during motor learning. Brain Res. *128*, 309–328. https://doi.org/10.1016/0006-8993(77)90997-0.

65. Tzingounis, A.V., and Wadiche, J.I. (2007). Glutamate transporters: confining runaway excitation by shaping synaptic transmission. Nat. Rev. Neurosci. *8*, 935–947. https://doi.org/10.1038/nrn2274.

66. Rothstein, J.D., Patel, S., Regan, M.R., Haenggeli, C., Huang, Y.H., Bergles, D.E., Jin, L., Dykes Hoberg, M., Vidensky, S., Chung, D.S., et al. (2005). Beta-lactam antibiotics offer neuroprotection by increasing glutamate transporter expression. Nature *433*, 73–77. https://doi.org/10.1038/nature03180.

67. Rothstein, J.D., Martin, L., Levey, A.I., Dykes-Hoberg, M., Jin, L., Wu, D., Nash, N., and Kuncl, R.W. (1994). Localization of neuronal and glial glutamate transporters. Neuron *13*, 713–725. https://doi.org/10.1016/0896-6273(94)90038-8.

68. Leung, T.C.H., Lui, C.N.P., Chen, L.W., Yung, W.H., Chan, Y.S., and Yung, K.K.L. (2012). Ceftriaxone Ameliorates Motor Deficits and Protects Dopaminergic Neurons in 6-Hydroxydopamine-Lesioned Rats. ACS Chem. Neurosci. *3*, 22–30. https://doi.org/10.1021/cn200072h.

69. Rebec, G.V. (2013). Dysregulation of corticostriatal ascorbate release and glutamate uptake in transgenic models of Huntington's disease. Antioxidants Redox Signal. *19*, 2115–2128. https://doi.org/10.1089/ars.2013.5387.

70. Takayasu, Y., Iino, M., Takatsuru, Y., Tanaka, K., and Ozawa, S. (2009). Functions of glutamate transporters in cerebellar Purkinje cell synapses. Acta Physiol. *197*, 1–12. https://doi.org/10.1111/j.1748-1716.2009.02019.x.

71. Han, K.-S., Chen, C.H., Khan, M.M., Guo, C., and Regehr, W.G. (2020). Climbing fiber synapses rapidly and transiently inhibit neighboring Purkinje cells via ephaptic coupling. Nat. Neurosci. *23*, 1399–1409. https://doi.org/10.1038/s41593-020-0701-z.

72. Conner, S.D., and Schmid, S.L. (2003). Differential requirements for AP-2 in clathrin-mediated endocytosis. J. Cell Biol. *162*, 773–779. https://doi.org/10.1083/jcb.200304069.

73. Garafalo, S.D., Luth, E.S., Moss, B.J., Monteiro, M.I., Malkin, E., and Juo, P. (2015). The AP2 clathrin adaptor protein complex regulates the abundance of GLR-1 glutamate receptors in the ventral nerve cord of Caenorhabditis elegans. Mol. Biol. Cell *26*, 1887–1900. https://doi.org/10.1091/mbc.E14-06-1048.

74. Koscielny, A., Malik, A.R., Liszewska, E., Zmorzynska, J., Tempes, A., Tarkowski, B., and Jaworski, J. (2018). Adaptor Complex 2 Controls Dendrite Morphology via mTOR-Dependent Expression of GluA2. Mol. Neurobiol. *55*, 1590–1606. https://doi.org/10.1007/s12035-017-0436-3.

75. Li, P., Merrill, S.A., Jorgensen, E.M., and Shen, K. (2016). Two Clathrin Adaptor Protein Complexes Instruct Axon-Dendrite Polarity. Neuron *90*, 564–580. https://doi.org/10.1016/j.neuron.2016.04.020.

76. Leto, K., Arancillo, M., Becker, E.B.E., Buffo, A., Chiang, C., Ding, B., Dobyns, W.B., Dusart, I., Haldipur, P., Hatten, M.E., et al. (2016). Consensus Paper: Cerebellar Development. Cerebellum *15*, 789–828. https://doi.org/10.1007/s12311-015-0724-2.

77. Hills, L.B., Masri, A., Konno, K., Kakegawa, W., Lam, A.T.N., Lim-Melia, E., Chandy, N., Hill, R.S., Partlow, J.N., Al-Saffar, M., et al. (2013). Deletions in GRID2 lead to a recessive syndrome of cerebellar ataxia and tonic upgaze in humans. Neurology *81*, 1378–1386. https://doi.org/10.1212/WNL.0b013e3182a841a3.

78. Miyoshi, Y., Yoshioka, Y., Suzuki, K., Miyazaki, T., Koura, M., Saigoh, K., Kajimura, N., Monobe, Y., Kusunoki, S., Matsuda, J., et al. (2014). A New Mouse Allele of Glutamate Receptor Delta 2 with Cerebellar Atrophy and Progressive Ataxia. PLoS One *9*, e107867. https://doi.org/10.1371/journal.pone.0107867.

79. Zuo, J., De Jager, P.L., Takahashi, K.A., Jiang, W., Linden, D.J., and Heintz, N. (1997). Neurodegeneration in Lurcher mice caused by mutation in delta2 glutamate receptor gene. Nature *388*, 769–773. https://doi.org/10.1038/42009.

80. Hall, R.A., and Soderling, T.R. (1997). Quantitation of AMPA receptor surface expression in cultured hippocampal neurons. Neuroscience *78*, 361–371. https://doi.org/10.1016/s0306-4522(96)00525-8.

81. Matsuda, S., and Yuzaki, M. (2002). Mutation in hotfoot-4J mice results in retention of δ2 glutamate receptors in ER. Eur. J. Neurosci. *16*, 1507–1516. https://doi.org/10.1046/j.1460-9568.2002.02219.x.

82. Soykan, T., Kaempf, N., Sakaba, T., Vollweiter, D., Goerdeler, F., Puchkov, D., Kononenko, N.L., and Haucke, V. (2017). Synaptic Vesicle Endocytosis Occurs on Multiple Timescales and Is Mediated by Formin-Dependent Actin Assembly. Neuron *93*, 854–866.e4. https://doi.org/10.1016/j.neuron.2017.02.011.

83. Custer, S.K., Garden, G.A., Gill, N., Rueb, U., Libby, R.T., Schultz, C., Guyenet, S.J., Deller, T., Westrum, L.E., Sopher, B.L., and La Spada, A.R. (2006). Bergmann glia expression of polyglutamine-expanded ataxin-7 produces neurodegeneration by impairing glutamate transport. Nat. Neurosci. *9*, 1302–1311. https://doi.org/10.1038/nn1750.

84. Chuang, C.-Y., Yang, C.-C., Soong, B.-W., Yu, C.-Y., Chen, S.-H., Huang, H.-P., and Kuo, H.-C. (2019). Modeling spinocerebellar ataxias 2 and 3 with iPSCs reveals a role for glutamate in disease pathology. Sci. Rep. *9*, 1166. https://doi.org/10.1038/s41598-018-37774-2.

85. Hund, T.J., Koval, O.M., Li, J., Wright, P.J., Qian, L., Snyder, J.S., Gudmundsson, H., Kline, C.F., Davidson, N.P., Cardona, N., et al. (2010). A β(IV)-spectrin/CaMKII signaling complex is essential for membrane excitability in mice. J. Clin. Invest. *120*, 3508–3519. https://doi.org/10.1172/jci43621.

86. Liang, R., Liu, X., Wei, L., Wang, W., Zheng, P., Yan, X., Zhao, Y., Liu, L., and Cao, X. (2012). The modulation of the excitability of primary sensory neurons by Ca^{2+}-CaM-CaMKII pathway. Neurol. Sci. *33*, 1083–1093. https://doi.org/10.1007/s10072-011-0907-7.

87. Carlier, E., Dargent, B., De Waard, M., and Couraud, F. (2000). Na+ Channel Regulation by Calmodulin Kinase II in Rat Cerebellar Granule Cells. Biochem. Biophys. Res. Commun. *274*, 394–399. https://doi.org/10.1006/bbrc.2000.3145.

88. Zybura, A.S., Baucum, A.J., Rush, A.M., Cummins, T.R., and Hudmon, A. (2020). CaMKII enhances voltage-gated sodium channel Nav1. J. Biol. Chem. *295*, 11845–11865. https://doi.org/10.1074/jbc.RA120.014062.

89. Lorenzetto, E., Caselli, L., Feng, G., Yuan, W., Nerbonne, J.M., Sanes, J.R., and Buffelli, M. (2009). Genetic perturbation of postsynaptic activity regulates synapse elimination in developing cerebellum. Proc. Natl. Acad. Sci. USA *106*, 16475–16480. https://doi.org/10.1073/pnas.0907298106.

90. Crepel, F., and Mariani, J. (1976). Multiple innervation of purkinje cells by climbing fibers in the cerebellum of the weaver mutant mouse. J. Neurobiol. *7*, 579–582. https://doi.org/10.1002/neu.480070610.

91. Crepel, F., Delhaye-Bouchaud, N., Guastavino, J.M., and Sampaio, I. (1980). Multiple innervation of cerebellar Purkinje cells by climbing fibres

in staggerer mutant mouse. Nature *283*, 483–484. https://doi.org/10.1038/283483a0.

92. Mariani, J., Crepel, F., Mikoshiba, K., Changeux, J.P., Sotelo, C., and Boycott, B.B. (1977). Anatomical, Physiological and biochemical studies of the cerebellum from *reeler* mutant mouse. Philos. Trans. R. Soc. Lond. B Biol. Sci. *281*, 1–28. https://doi.org/10.1098/rstb.1977.0121.

93. White, J.J., and Sillitoe, R.V. (2017). Genetic silencing of olivocerebellar synapses causes dystonia-like behaviour in mice. Nat. Commun. *8*, 14912. https://doi.org/10.1038/ncomms14912.

94. Cook, A.A., Leung, T.C.S., Rice, M., Nachman, M., Zadigue-Dubé, É., and Watt, A.J. (2023). Endosomal Dysfunction Contributes to Cerebellar Deficits in Spinocerebellar Ataxia Type 6 (Cold Spring Harbor Laboratory).

95. Johnson, E.M., Craig, E.T., and Yeh, H.H. (2007). TrkB is necessary for pruning at the climbing fibre-Purkinje cell synapse in the developing murine cerebellum. J. Physiol. *582*, 629–646. https://doi.org/10.1113/jphysiol.2007.133561.

96. Massaad, C.A., and Klann, E. (2011). Reactive Oxygen Species in the Regulation of Synaptic Plasticity and Memory. Antioxidants Redox Signal. *14*, 2013–2054. https://doi.org/10.1089/ars.2010.3208.

97. Wang, Y.T., and Linden, D.J. (2000). Expression of cerebellar long-term depression requires postsynaptic clathrin-mediated endocytosis. Neuron *25*, 635–647. https://doi.org/10.1016/s0896-6273(00)81066-1.

98. Wagner, W., Lippmann, K., Heisler, F.F., Gromova, K.V., Lombino, F.L., Roesler, M.K., Pechmann, Y., Hornig, S., Schweizer, M., Polo, S., et al. (2019). Myosin VI Drives Clathrin-Mediated AMPA Receptor Endocytosis to Facilitate Cerebellar Long-Term Depression. Cell Rep. *28*, 11–20.e9. https://doi.org/10.1016/j.celrep.2019.06.005.

99. Takeuchi, T., Ohtsuki, G., Yoshida, T., Fukaya, M., Wainai, T., Yamashita, M., Yamazaki, Y., Mori, H., Sakimura, K., Kawamoto, S., et al. (2008). Enhancement of Both Long-Term Depression Induction and Optokinetic Response Adaptation in Mice Lacking Delphilin. PLoS One *3*, e2297. https://doi.org/10.1371/journal.pone.0002297.

100. Roche, K.W., Ly, C.D., Petralia, R.S., Wang, Y.-X., McGee, A.W., Bredt, D.S., and Wenthold, R.J. (1999). Postsynaptic Density-93 Interacts with the δ2 Glutamate Receptor Subunit at Parallel Fiber Synapses. J. Neurosci. *19*, 3926–3934. https://doi.org/10.1523/jneurosci.19-10-03926.1999.

101. Tyanova, S., Temu, T., and Cox, J. (2016). The MaxQuant computational platform for mass spectrometry-based shotgun proteomics. Nat. Protoc. *11*, 2301–2319. https://doi.org/10.1038/nprot.2016.136.

STAR★METHODS

KEY RESOURCES TABLE

REAGENT or RESOURCE	SOURCE	IDENTIFIER
Antibodies		
mouse anti-AP-2α	BD Biosciences	Cat# 610501; RRID: AB_397867
mouse anti-AP-2μ (WB)	BD Biosciences	Cat# 611350; RRID: AB_398872
mouse anti-AP-2α (IHC)	Abcam	Cat# ab2730; RRID: AB_303255
mouse anti-β-actin	Sigma-Aldrich	Cat# A-5441; RRID: AB_476744
chicken anti-calbindin	Novus Biologicals	Cat# NBP2-50028; RRID: AB_2938765
mouse anti-calbindin	Proteintech	Cat# 66394-1-Ig; RRID: AB_2881769
mouse anti-clathrin heavy chain	homemade	N/A
rabbit anti-cleaved caspase3	Cell Signaling	Cat# 9661S; RRID: AB_2341188
rabbit anti-FOXP2	Proteintech	Cat# 20529-1-AP; RRID: AB_10695756
chicken anti-GFP	Abcam	Cat#ab13970; RRID: AB_300798
rabbit anti-GLT-1	Santa Cruz Biotechnology	Cat#sc-365634; RRID: AB_10844832
rabbit anti-GLURδ2 (WB)	Abcam	Cat# ab190358; RRID: N/A
rabbit anti-GLURδ2 (IHC)	Novus Biologicals	Cat# NBP2-31723; RRID: N/A
rabbit anti-GRID1IP	Novus Biologicals	Cat# NBP1-94174; RRID: AB_11008710
Streptavidin peroxidase conjugated	Thermo Fisher Scientific	Cat# S911; RRID: N/A
rabbit anti-synaptotagmin1-oyster650	Synaptic Systems	Cat# 105103C5; RRID: AB_2619766
mouse anti-synaptotagmin1	Synaptic Systems	Cat# 105 011; RRID: AB_887832
rabbit anti-VGAT-oyster550	Synaptic Systems	Cat #131 103C3; RRID: AB_887867
guinea pig anti-VGAT	Synaptic Systems	Cat# 131 004; RRID: AB_887873
guinea pig anti-Vglut1	Synaptic Systems	Cat# 135304; RRID: AB_887878
guinea pig anti-Vglut2	Synaptic Systems	Cat# 135404; RRID: AB_887884
chicken anti-vimentin	Novus Biologicals	Cat# NB300-223SS; RRID: AB_922758
goat anti-chicken Alexa 488	Thermo Fisher Scientific	Cat# A11039; RRID: AB_2534096
goat anti-chicken Alexa 568	Thermo Fisher Scientific	Cat# A11041; RRID: AB_2534098
goat anti-chicken Alexa 647	Thermo Fisher Scientific	Cat# A21449; RRID: AB_2535866
goat anti-guinea pig Alexa 488	Thermo Fisher Scientific	Cat# A11073; RRID: AB_2534117
goat anti-guinea pig Alexa 647	Thermo Fisher Scientific	Cat# A21450; RRID: AB_2535867
goat anti-mouse Alexa 488	Thermo Fisher Scientific	Cat# A11029; RRID: AB_2534088
goat anti-mouse Alexa 568	Thermo Fisher Scientific	Cat# A11031; RRID: AB_144696
goat anti-mouse Alexa 647	Thermo Fisher Scientific	Cat# A21236; RRID: AB_2535805
goat anti-rabbit Alexa 488	Thermo Fisher Scientific	Cat# A11034; RRID: AB_2576217
goat anti-rabbit Alexa 568	Thermo Fisher Scientific	Cat# A11011; RRID: AB_143157
goat anti-rabbit Alexa 647	Thermo Fisher Scientific	Cat# A21245; RRID: AB_2535813
goat anti-Rabbit IgG (H + L) peroxidase-conjugated	Sigma-Aldrich	Cat# A0545; RRID: AB_257896
rabbit anti-Chicken IgG (H + L) peroxidase-conjugated	Merk Millipore	Cat# AP162P; RRID: AB_91653
rabbit anti-Mouse IgG (H + L) peroxidase-conjugated	Sigma-Aldrich	Cat# A9044; RRID: AB_258431
normal rabbit IgG	Cell Signaling	Cat#2729S; RRID: AB_1031062
Viruses		
AAV1/2-Ef1α-DIO EYFP	Karl Deisseroth (unpublished)	Addgene viral prep #27056-AAV1, RRID: Addgene_27056

(*Continued on next page*)

Continued

REAGENT or RESOURCE	SOURCE	IDENTIFIER
AAV2/rh10-L7-6-EGFP-WPRE	custom-produced, this paper	To be deposited on Addgene upon publication: https://www.addgene.org/Günter_Schwarz/
AAV2/rh10-L7-6-EGFP-P2A-Cre-WPRE	custom-produced, this paper	To be deposited on Addgene upon publication: https://www.addgene.org/Günter_Schwarz/
ssAAV-9/2-mCaMKIIα-jGCaMP7f-WPRE-bGHp(A)	Viral Vector Facility Zürich	jGCaMP7f: Addgene #104483
ssAAV-1/2-hEF1α-dlox-dAPEX2(rev)-dlox-WPRE-hGHp(A)	Viral Vector Facility Zürich	pAAV-DIO-dAPEX2: Addgene #117174
Chemicals, peptides, and recombinant proteins		
Ascorbic acid	Carl Roth	3525.1
β-mercaptoethanol	Carl Roth	4227.1
bis-tris propane	Sigma Aldrich	B6755
Bovine serum albumin (BSA)	Sigma Aldrich	A7906
Bromophenol (0.03%)	Sigma Aldrich	B5525
BSA (fatty acid free)	Sigma Aldrich	A6003
Calcium chloride ($CaCl_2$)	Carl Roth	5239.2
Ceftriaxone disodium salt hemi(heptahydrate)	Sigma Aldrich	C5793
D-Glucose	Sigma Aldrich	G5767
Dimethyl sulfoxide (DMSO)	Carl Roth	A994.2
DMEM	Thermo Fisher Scientific	A14430
dPBS	Gibco	14190250
DNAse	Sigma Aldrich	150000U
EBSS	Thermo Fisher Scientific	14155–048
Fetal bovine serum (FBS)	Merck Millipore	S0115
FM™1-43FX	Invitrogen™	F35355
Gelatin from porcine skin	Sigma Aldrich	G2500
GlutaMAX™	Thermo Fisher Scientific	35050–061
Glycerol	Carl Roth	7530.1
HBSS	Gibco	14175–053
Heparin	Sigma Aldrich	H4784
HEPES	Thermo Fisher Scientific	15630–080
Horse serum (heat-inactivated)	Gibco	26050088
IGEPAL CA-630	Sigma Aldrich	I8896
Insulin	Life Technologies	12585–014
Ketamin hydrochloride	Sigma Aldrich	K2753
Kynurenic acid	Tocris	3694
Magnesium-ATP (Mg-ATP)	Sigma Aldrich	20–113
Magnesium chloride ($MgCl_2$)	Carl Roth	2189.1
Magnesium sulfate ($MgSO_4$)	Carl Roth	T888.1
MEM	Sigma Aldrich	7278
Penicillin/Streptomycin (P/S)	Thermo Fisher Scientific	15140–122
Phosphocreatine	Tocris	4325
Pitstop	Abcam	ab120687
Potassium chloride (KCl)	Karl Roth	6781.1
Potassium gluconate	Merk Millipore	299-27-4

(*Continued on next page*)

Continued

REAGENT or RESOURCE	SOURCE	IDENTIFIER
Protease and phosphatase inhibitor mini tablets	Thermo Fisher Scientific	A32959
Rompun 2% (Xylazin)	Bayer	KP0BZPE
Saponin	Sigma aldrich	47036
SDS	Carl Roth	2326.2
Sodium bicarbonate ($NaHCO_3$)	Carl Roth	8551.1
Sodium chloride (NaCl)	Carl Roth	3957.1
Sodium deoxycholate	Thermo Fisher Scientific	89904
Sodium-GTP (Na-GTP)	Merk Millipore	G3776
Sodium hydrogen phosphate (NaH_2HPO_4)	Carl Roth	3904.1
Sodium pyruvate	Thermo Fisher Scientific	11360–039
Soybean trypsin inhibitor	Merck Millipore	10109886001
Transferrin, Alexa Fluor 488 conjugated	Thermo Fisher Scientific	T13342
Tris	VWR	28.808.294
Tris-HCl	Sigma Aldrich	T3253
Triton X-100	Sigma Aldrich	9036-19-5
Tween 20	VWR	663684B
Trypsin	Sigma Aldrich	T1005
Critical commercial assays		
RNAScope® Fluorescent Multiplex Detection Reagents	Advanced Cell Diagnostic	323110
Mm-Grid2ip-C1 RNA probe	Advanced Cell Diagnostic	Cat# 1253061-C1
NEBuilder HiFi DNA Assembly	New England Biolabs	Cat# E2621S
Deposited data		
Proteomics data	ProteomeXchange	PRIDE: PXD050090 and PXD050031
Experimental models: Organisms/strains		
Ap2m1^{flox}	Prof. Dr. Volker Haucke, FMP, Berlin	Kononenko et al., 2014
L7^{Cre} (provided by Prof. Rugarli, Cologne)	The Jackson Laboratory	RRID: MGI: J:66884
B6.Cg-Gt(ROSA)26Sortm14(CAG-tdTomato)Hze (Ai9-tdTomato (provided by Prof. Bergami, Cologne)	The Jackson Laboratory	RRID: MGI: J:155793
Oligonucleotides		
Primers for Ai9, see Table S3	The Jackson Laboratory	N/A
Primers for *Ap2m1*^{flox}, see Table S3	Kononenko et al., 2014	N/A
Primers for L7^{Cre}, see Table S3	The Jackson Laboratory	N/A
Recombinant DNA		
Plasmid: pAAV/L7-6-GFP-WPRE	Addgene	Addgene plasmid # 126462, RRID: Addgene_126462
Plasmid: pAAV-hSyn-mScarlet	Addgene	Addgene plasmid #131001, RRID:Addgene_131001
Plasmid: pAAV.CMV.HI.eGFP-Cre.WPRE.SV40	Addgene	Addgene plasmid # 105545, RRID: Addgene_105545
Plasmid: pAdDeltaF6	Addgene	Addgene plasmid #112867, RRID: Addgene_112867
pAAV2/rh10	Addgene	Addgene plasmid # 112866, RRID: Addgene_112866
Software and algorithms		
Amira Software 2020.2 Thermo Fisher Scientific	Thermo Fisher Scientific	http://www.fei.com/software/amira-3d-for-life-sciences/RRID: SCR_007353

(*Continued on next page*)

Continued

REAGENT or RESOURCE	SOURCE	IDENTIFIER
Aperio ImageScope version 12.4.3.5008	Leica Microsystems	https://www.leicabiosystems.com/aperio-imagescope/RRID: SCR_020993
pClamp	Molecular Devices	http://www.moleculardevices.com/products/software/pclamp.html RRID: SCR_11323
Excel – Office 2021	Microsoft	https://www.microsoft.com/RRID: SCR_016137
Fiji version 1.53	Wayne Rasband, National Institute of Health, Bethesda, USA	https://imagej.net/RRID: SCR_002285
GraphPad Prism version 9.5.1	GraphPad	http://www.graphpad.com/RRID: SCR_002798
Inkscape 1.3.2	Inkscape	https://inkscape.org/RRID: SCR_014479
LAS X Life Science Microscope Software	Leica Microsystems	https://www.leica-microsystems.com/products/microscope-software/p/leica-las-x-ls/RRID: SCR_013673
R	The R Foundation of Statistical Computing, Vienna, AT	https://www.r-project.org/foundation RRID: SCR_000432
AutoGaitA	Hosseini team	https://github.com/mahan-hosseini/AutoGaitA

EXPERIMENTAL MODEL AND STUDY PARTICIPANT DETAILS

Mice were kept on a mixed C57BL6/NRj:C57BL6/6J background. Mice were analyzed between 1 and 3 months of age (the exact age is indicated in Results and Figure legends). Mice were group-housed in polycarbonate cages with 12hr day/light cycles and water and food were available *ad libitum*. All experiments were performed in accordance with the regulations issued by the Federal Government of Germany, European Union legislation and the regulations of the University of Cologne. The experimental procedures were approved by the Landesamt für Natur, Umwelt und Verbraucherschutz Nordrhein-Westfalen (AZ 81-02.04.2020.A418, AZ 81-02.04.2021.A067, AZ 81-02.04.2021.A132 and AZ 81-02.04.2022.A116). *Ap2m1*^{flox} mice have been previously described (Kononenko et al., 2014) and were crossed in this study with *L7*^{Cre} mice (Barski et al., 2000) to generate AP-2 cKO mice (Genotype: *L7*$^{Cre/+}$;*Ap2m1*$^{flox/flox}$). Mice with genotypes *Ap2m1*$^{wt/wt}$; L7^{Cre} (i.e., WT) and *Ap2m1*$^{fl/fl}$; L7^{Cre} (i.e., AP-2 cKO) were used in the current study. In a subset of AP-2 cKO mice, the tdTomato expression was driven by crossing *L7*$^{Cre/+}$;*Ap2m1*$^{flox/flox}$ mice with the reporter mouse line Ai9 (Madisen et al., 2010). For comparison of AP-2 cKO and control mice, littermates from several litters were used. Both female and male mice were used for primary neurons culture, cerebellar acute slices, cerebellar organotypic slices, immunostaining, immunoblotting, multiplex RNA *in situ* analysis, behavioral experiments, proteomics, electrophysiology and stereotactic viral vector injections. No influence of sex on the phenotype of the mice was detected. Only male mice were used for MRI body composition measurements. C57BL6/NRj WT mice were used for MS and Co-IPs WT experiments. Primary cerebellar neuron were prepared from P8 WT and AP-2 cKO mice. OTCs were prepared from P8 and/or 1-month-old WT and AP-2 cKO mice. Recombinant AAV particles were prepared in HEK293T cells (DSMZ no. ACC 635). HEK cells were regularly tested for mycoplasma contamination.

METHOD DETAILS

Tissue processing and immunohistochemical analysis

Adult mice were anesthetized with an intraperitoneal injection of Ketamin/Rompun and transcardially perfused with Ringer solution (0.85% NaCl, 0.025% KCl, 0.02% $NaHCO_3$, 0.01% heparin, pH 6.9) followed by 4% PFA in PBS (pH 7.4). Brains were dissected and post-fixed in 4% PFA overnight at 4°C and subsequently placed in a mixture of 20% (vol/vol) glycerol and 2% (vol/vol) dimethyl sulfoxide (VWR international) in 0.4M PBS for cryoprotection. 40 μm sagittal cryosections were obtained and free-floating sections were collected in the same cryoprotective solution mentioned above and stored at −80°C until further use. For immunofluorescent staining, brain sections were washed once in PBS for 10 min and incubated in blocking solution containing 10% normal goat serum (NGS) in PBS plus 0.5% Triton X-100 (0.5% PBT) for 1h at room temperature (RT). Sections were incubated with primary antibodies for 48 h at 4°C in 0.3% PBT plus 3% NGS and afterward washed 3 times for 5–10 min each in 0.3% PBT. Sections were then incubated with secondary antibodies for 2hr in the dark at RT in 0.3% PBT plus 3% NGS and washed 3 times for 5–10 min each in 0.3% PBT. Sections were finally mounted on gelatin-coated glass slides with Immu-Mount (Epredia). A list of primary and secondary antibodies is provided in the Key Resource Table. The following primary antibodies dilutions were used: 1:1000 for chicken anti-Calbindin, 1:500

for mouse anti-calbindin, 1:1000 for chicken anti-GFP, 1:300 for rabbit anti- Cleaved Caspase3, 1:200 for mouse anti-AP-2α, 1:200 for rabbit anti-GRID2IP, 1:200 for rabbit anti-GLURδ2, 1:1000 for guinea pig anti-Vglut2, 1:500 for guinea pig anti-Vglut1, 1:300 for mouse anti-AP-2μ and 1:500 for rabbit anti-FOXP2. All Alexa fluorophore-conjugated secondary antibodies were used at a 1:500 dilution.

For immunofluorescence of cerebellar acute slices or organotypic slice cultures, sections were permeabilized in 0.5% Triton X-100 (0.5% PBT) for 30 min at RT and then processed as described above. The following primary antibodies dilutions were used: 1:300 for chicken anti-calbindin, 1:300 for mouse anti-calbindin and 1:300 for mouse anti-synaptotagmin1. All Alexa fluorophore-conjugated secondary antibodies were used at a 1:500 dilution.

Nissl staining

For Cresyl-violet staining 40 μm sagittal sections from 1-, 2- and 3-month-old AP-2 cKO mice and control littermates were mounted on SuperFrost Ultra plus microscope slides (Thermo Scientific) and dried overnight. Sections were stained following previously described protocol (Kononenko et al., 2017).

Immunoblotting analysis

2-month-old mice were sacrificed via cervical dislocation. Brains were isolated and the cerebellum was dissected, shock-frozen in liquid nitrogen and stored at −80°C until tissue lysis. For immunoblot analysis of cerebellar organotypic cultures, slices were collected at DIV21, shock-frozen in liquid nitrogen and stored at −80°C until tissue lysis. Samples were homogenized in RIPA buffer (50 mM Tris pH 8.0, 150 mM NaCl, 1.0% IGEPAL CA-630, 0.5% Sodium deoxycholate, 0.1% SDS) containing phosphatase inhibitor (Thermo Scientific) and protease inhibitor (Roche) using a Wheaton Potter-Evehjem Tissue Grinder. Subsequently, samples were sonicated, incubated on ice for 45 min and centrifuged at 13000 rpm for 15 min at 4°C. Supernatant concentration was assessed using Bradford assay (Sigma) and samples were mixed with 4x SDS buffer (250 mM Tris-HCL, 1% (w/v) SDS, 40% (v/v) Glycerol, 4% (v/v) β-mercaptoethanol, 0.03% Bromophenol) and boiled for 5 min at 95°C. 10–20 μg of protein per sample were loaded onto SDS-page gels for protein separation and afterward transferred onto nitrocellulose membrane via full-wet transfer assay (Bio-rad). Membranes were blocked in 5% milk or bovine serum albumin (BSA) in TBS (20 mM Tris pH = 7.6, 150 mM NaCl) containing 1% Tween (TBS-T) at RT for 1h before incubation with primary antibodies in TBS overnight at 4°C. Afterward, membranes were washed 3 times with TBS-T for 10 min at RT before incubation with HRP-tagged secondary antibodies for 1h at RT. Membranes were finally washed 3 times with TBS-T for 10 min at RT. A list of primary and secondary antibodies is provided in the Key Resource Table. Protein levels were visualized using ECL-based autoradiography film system (Super RX-N, Fujifilm) or ChemiDocTM Imaging system (BioRad) and analyzed using Gel Analyzer plugin from ImageJ (Fiji). Protein levels were first normalized to loading control and then to the appropriate control. The following primary antibody dilutions were used: 1:1000 for mouse anti- AP-2α, 1:1000 for mouse anti-AP-2μ, 1:1000 for chicken anti-calbindin, 1:1000 for rabbit anti-GRID2IP, 1:1000 for rabbit anti-GLT-1, 1:2500 for mouse anti-β-actin and 1: 5000 for Streptavidin-HRP. All HRP-conjugated secondary antibodies were used at a 1:10 000 dilution.

Co-immunoprecipitation

For immunoprecipitation experiments, 20 μL Dynabeads Protein G (Thermo Fischer Scientific) were coated with 2μg antibody targeting the protein of interest and corresponding IgG as a negative control (see Key Resource Table). Dynabeads storing solution was replaced with 100 μL PBS and 2μg of antibody was added. The beads were incubated with the antibody for 2-3h at 4°C on a shaker and then washed with 200μL PBS to remove excessive antibody. 8-week-old WT mice were sacrificed via cervical dislocation, brains were isolated and the cerebellum was dissected and homogenized in co-IP buffer (50 mM Tris-HCl pH=7.4, 1% NP-40/Igepal, 100 mM NaCl, 2 mM $MgCl_2$) supplemented with Proteinase Inhibitor (Roche) und Phosphatase Inhibitor (ThermoScientific) using a Wheaton Potter-Elvehjem Tissue Grinder. Samples were sonicated and incubated on ice for 45 min before being centrifuged at 13000 rpm for 20 min at 4°C. Protein concentration was assessed using Bradford assay (Sigma). An equal amount of protein was added to the antibody-coupled Dynabeads and control IgG for overnight incubation at 4°C on a shaker. Afterward, the lysates were removed and Dynabeads were washed 3 times with co-IP buffer before being dissolved in a mixture of 20 μL co-IP buffer and 20 μL 4x SDS buffer and boiled at 95°C for 5 min. Precipitation of proteins was detected via SDS-page gel.

Mass spectrometry (MS) analysis of AP-2α binding partners in the cerebellum

8-week-old WT mice were sacrificed via cervical dislocation. Brains were isolated and the cerebellum was dissected for MS analysis. Cerebellar tissue was homogenized in co-IP buffer, as described in the previous section. Samples were boiled at 95°C for 5 min and then loaded onto SDS-PAGE gels, reduced (DTT), and alkylated (CAA). Digestion was performed using trypsin at 37°C overnight. Peptides were extracted and purified using Stagetips. Eluted peptides were dried in vacuo, resuspended in 1% formic acid/4% acetonitrile and stored at −20°C before MS measurement. All samples were analyzed by the CECAD proteomics facility as previously described.[37]

Proteomics

For total proteome analysis 2.month-old mice were sacrificed via cervical dislocation. Brains were extracted and the cerebellum was dissected, shock frozen in liquid nitrogen and stored at −80°C until further use. Cerebellar tissue was lysed in Urea lysis buffer (50 mM

TEAB, 8M Urea, 50x Protease inhibitor), sonicated and centrifuged at 20000g for 15 min. Protein concentration was assessed using Bradford assay (Sigma). Samples were processed with in-solution digestion. All solutions were provided by the CECAD proteomics facility. For each sample, 50 μg of protein were transferred into fresh tubes, reduced with 5 mM DTT for 1h at 25°C and subsequently alkylated with 40 mM CAA for 30 min in the dark. Protein digestion was performed by incubating samples in LysC at an enzyme:substrate ratio of 1:75 for 4h at 25°C. Samples were afterward diluted with 50 mM TEAB to achieve a final concentration of 2 M Urea and then incubated overnight at 25°C in 1:75 ratio Trypsin. The following day, samples were acidified with formic acid (final concentration 1%). Peptides were extracted and purified using Stagetips. First, StageTips were equilibrated with washes in methanol, buffer B (80% acetonitril; 0.1% (v/v) formic acid) and twice buffer A (dH_2O; 0.1% (v/v) formic acid). Each wash was followed by centrifugations at 2600 rpm for 1–2 min. For peptide purification, samples were centrifuged at 13000 rpm for 5 min and the loaded onto StageTips. Samples were centrifuged at 2600 rpm for 5 min, StageTips were washed with buffer A and centrifuged at 2 600 for 3 min. Finally, StageTips were washed twice with buffer B and each time centrifuged at 2 600 for 3 min and stored at 4°C untill submission to the CECAD proteomics facility for further processing.

Samples were analyzed by the CECAD Proteomics Facility on an Orbitrap Exploris 480 (Thermo Scientific, granted by the German Research Foundation under INST 1856/71-1 FUGG) mass spectrometer equipped with a FAIMSpro differential ion mobility device that was coupled to an UltiMate 3000 (Thermo Scientific). Samples were loaded onto a precolumn (Acclaim 5μm PepMap 300 μm Cartridge) for 2 min at 15 μl flow before being reverse flushed onto an in-house packed analytical column (30 cm length, 75 μm inner diameter, filled with 2.7 μm Poroshell EC120 C18, Agilent). Peptides were chromatographically separated at a constant flow rate of 300 nL/min and the following gradient: initial 6% B (0.1% formic acid in 80% acetonitrile), up to 32% B in 72 min, up to 55% B within 7.0 min and up to 95% solvent B within 2.0 min, followed by column wash with 95% solvent B and re-equilibration to initial condition. The FAIMS pro was operated at −50V compensation voltage and electrode temperatures of 99.5°C for the inner and 85°C for the outer electrode. For the Gas-phase fractionated library, a pool generated from all samples was analyzed in six individual runs covering the range from 400 m/z to 1000 m/z in 100 m/z increments. For each run, MS1 was acquired at 60k resolution with a maximum injection time of 98 msec and an AGC target of 100%. MS2 spectra were acquired at 30k resolution with a maximum injection time of 60 msec. Spectra were acquired in staggered 4 m/z windows, resulting in nominal 2 m/z windows after deconvolution using ProteoWizard (Chambers, 2012). For the samples, MS1 scans were acquired from 399 m/z to 1001 m/z at 15k resolution. Maximum injection time was set to 22 msec and the AGC target to 100%. MS2 scans ranged from 400 m/z to 1000 m/z and were acquired at 15 k resolution with a maximum injection time of 22 ms and an AGC target of 100%. DIA scans covering the precursor range from 400 to 1000 m/z and were acquired in 60 x 10 m/z windows with an overlap of 1 m/z. All scans were stored as centroid.

The gas-phase fractionated library was built in DIA-NN 1.8.1 (Demichev 2020) using A Swissprot mouse canonical database (UP589, downloaded 04/01/22) with settings matching acquisition parameters. Samples were analyzed in DIA-NN 1.8.1 as well using the previously generated library and identical database. DIA-NN was run with the additional command line prompts "—report-lib-info" and "—relaxed-prot-inf". Further output settings were: filtered at 0.01 FDR, N-terminal methionine excision enabled, maximum number of missed cleavages set to 1, min peptide length set to 7, max peptide length set to 30, min precursor m/z set to 400, max precursor m/z set to 1000, cysteine carbamidomethylation enabled as a fixed modification. Afterward, DIA-NN output was further filtered on library q-value and global q-value $\leq$ 0.01 and at least two unique peptides per protein using R (4.1.3). Finally, LFQ values calculated using the DIA-NN R-package. Afterward, analysis of results was performed in Perseus 1.6.15.[101] GO analysis of up and downregulated pathways in the cerebellum of 1- and 2-month-old mice was performed using ShinyGO v0.80 (South Dakota State University; Ge, Jung and Yao, 2020). Venn diagram analysis was performed using Venny2.1 (Oliveros, J.C. (2007–2015) Venny). An interactive tool for comparing lists with Venn's diagrams. https://bioinfogp.cnb.csic.es/tools/venny/index.html).

APEX proteomics

In order to study Purkinje cell-specific proteome in the mouse cerebellum, we used an enzyme-catalyzed proximity labeling approach combined with mass spectrometry-based proteomics. For proximity labeling within genetically targeted neurons, a Cre-dependent AAV expressing the engineered ascorbate peroxidase APEX2 (ssAAV-1/2-hEF1α-DIO-dAPEX2) was intracranially injected into the cerebellum of 6-week-old AP-2 cKO and control mice. For stereotactic surgery procedure see *Stereotactic viral injection* below. Three weeks after stereotactic surgery, injected mice were anesthetized with an intraperitoneal injection of Ketamin/Rompun and transcardially perfused with ice-cold cutting solution (92 mM N-Methyl-D-glucamine, 2.5 mM KCl, 30 mM $NaHCO_3$, 20 mM HEPES, 1.25 mM NaH_2PO_4, 2mM thiourea, 5 mM sodium ascorbate, 3 mM sodium pyruvate, 10 mM $MgSO_4$, 0.5 mM $CaCl_2$, 25 mM D-glucose, pH 7.4 and saturated with 95% O2/5%CO2). Afterward, the brain was rapidly extracted, the cerebellum isolated and chopped into 300 μm pieces with a tissue chopper (Cavey Laboratory Engineering Co. LTD). Chopped cerebellar tissue was incubated in ACSF (125.2 mM NaCl, 2.5 mM KCl, 26 mM $NaHCO_3$, 1.3 mM $MgCl_2$ 6 H_2O, 2.4 mM $CaCl_2$, 0.3 mM $NaHPO_4$, 0.3 mM KH_2PO_4 and 10mM D-glucose) supplemented with 0.5 mM biotinphenol (BP) at 37°C for 30 min (95%O_2/5% CO_2). Afterward, APEX labeling was intiated by the addition of 1 mM H_2O_2 to ACSF at room temperature. After 1 min, ACSF was discarded and exchanged with cold quenching buffer (ACSF supplemented with 10mM Trolox, 20 mM sodium ascorbate and 10 mM NaN_3) on ice. The tissue was washed twice with cold quenching buffer (in-between incubation times of 2 min) and twice more with cold PBS. Finally, samples were resuspended in 8M urea buffer supplemented with protease inhibitor and centrifuged for 15 min at 20000 g at room temperature. The supernatant was collected and transferred into fresh 1.5 mL Eppendorf tubes. The protein

concentration was measured and all samples were adjusted to reach the same concentration with 8M urea. Finally, an acetone precipitation protocol was applied. Briefly, samples were mixed with 4 times the volume of cold (−20°C) acetone, vortexed and incubated at −20°C for 3 h. Afterward, samples were centrifuged for 10 min at 15000 g at 4°C and the supernatant discarded. The protein pellet was washed twice with 80%–90% acetone (−20°C) and centrifuged for 10 min at 15000 g at 4°C. The supernatant was decanted and the acetone was allowed to evaporate at room temperature for approximatively 10 min. The pellet was resuspended in 5 μL/10μg protein of 6M urea in ABC solution and afterward sonicated. Samples were stored at −80°C until enrichment on SAV-beads and MS experiments. Biotinylated proteins were captured using Pierce High Capacity Streptavidin Agarose (Thermo Scientific, #20359). Briefly, the streptavidin bead slurry was washed three times with 1x PBS. The washed beads were then incubated with the protein sample overnight at 4°C with gentle tumbling. After incubation, the beads were washed extensively with 1x PBS (five washes). Finally, the beads were resuspended in a sufficient volume of 8M Urea solution to completely cover the beads, maximizing the yield of enriched proteins. Following protein capture, samples were processed according to the established proteomics protocol provided by the CECAD proteomics facility (mentioned above).

Adeno-associated viruses' generation

DNA constructs

pAAV/L7-6-EGFP-WPRE was generated from pAAV/L7-6-GFP-WPRE (a gift from Hirokazu Hirai, Addgene plasmid # 126462; http://n2t.net/addgene:126462; RRID:Addgene_126462) and the pAAV backbone from pAAV-hSyn-mScarlet (a gift from Karl Deisseroth, Addgene plasmid #131001; http://n2t.net/addgene:131001; RRID:Addgene_131001) using NEBuilder HiFi DNA Assembly (NEB). A P2A-Cre construct was generated from pAAV.CMV.HI.eGFP-Cre.WPRE.SV40 (a gift from James M. Wilson, Addgene plasmid # 105545; http://n2t.net/addgene:105545; RRID:Addgene_105545) by site directed mutagenesis using forward (GGCGACG TGGAGGAGAACCCCGGCCCCGCCGGCAGCATGTCCGGAGAGCAAAAGCTG) and reverse (TCTCCTCCACGTCGCCGGCCT GCTTCAGCAGGCTGAAGTTGGTGGCGCCGCTGCCCTTGTACAGCTCGTCCATGC) primers. Subsequently, pAAV/L7-6-EGFP-P2A-Cre-WPRE was generated using NEBuilder HiFi DNA Assembly. The plasmids pAdDeltaF6 (Addgene plasmid #112867; http://n2t.net/addgene:112867; RRID:Addgene_112867) and pAAV2/rh10 (Addgene plasmid # 112866; http://n2t.net/addgene:112866; RRID:Addgene_112866) were a gift from James M. Wilson. All DNA constructs were confirmed by Sanger sequencing (Eurofins).

rAAV2/rh10 preparation

Recombinant AAV2/rh10 particles were prepared in HEK293T cells (DSMZ no. ACC 635) by transfecting either pAAV/L7-6-EGFP-WPRE or pAAV/L7-6-EGFP-P2A-Cre-WPRE together with pAdDeltaF6 and pAAV2/rh10. Viral particles were precipitated with PEG/NaCl and cleared with chloroform extraction (Kimura et al., 2019). AAVs were purified by adapting scalable anion-exchange chromatography strategies (Dickerson, Argento, Pieracci, & Bakhshayeshi, 2021; Wang et al., 2019). Cleared AAVs were concentrated roughly 20-fold with pre-washed (PBS +0.001% (v/v) Poloxamer 188, Sigma Aldrich) 100 kDa Amicon filters (Merck/Millipore) and diluted 10-fold in buffer A (10 mM bis-tris-propane pH 9.0, 1 mM $MgCl_2$). AAVs were applied at a flow-rate of 3 mL/min to a self-packed 1 mL column (POROSTM HQ 50 μm strong anion exchange resin, Thermo Fisher Scientific), which was equilibrated in buffer A. After injection, the column was rinsed with 20 column volumes buffer A, washed with 20 column volumes 4% buffer B (10 mM bis-tris-propane pH 9.0, 1 mM $MgCl_2$, 1 M NaCl). AAVs were eluted with 35% buffer B. Eluted fractions were concentrated and buffer exchanged to PBS +0.001% (v/v) Poloxamer 188 using 100 kDa Amicon filters. Purity of viral preparations were assessed with SDS-PAGE/Colloidal Commassie staining and AAV titers determined using Gel green (Biotium) (Xu, DeVries, & Zhu, 2020).

Stereotactic viral vector injection

Stereotactic injections of AAV1/2-Ef1α-DIO-EYFP (Addgene viral prep # 27056-AAV1, titer ≥ $1x10^{13}$ vg/mL) were performed on 4-week-old AP-2 cKO mice and control littermates to label Purkinje cells with EYFP in a Cre-dependent manner. For AP-2μ acute deletion in the cerebellum, stereotactic injections of AAV2/rh10-L7-6-EFGP-WPRE control virus (titer 5.05 $*10^{13}$ GC/mL) or AAV2/rh10-L7-6-EFGP-P2A-Cre-WPRE (titer 5.04 $*10^{13}$ GC/mL) were performed on 6-week-old *Ap2m1*$^{flox/flox}$ mice. Injections with ssAAV-1/2-hEF1α-dlox-dAPEX2(rev)-dlox-WPRE-hGHp(A) were performed on 6-week-old AP-2 cKO and WT animals. Mice were weighed and anesthetized with an intraperitoneal injection of Ketamine (100 mg/kg)/Xylazine (20 mg/kg)/Acepromazine/Azaperon (3 mg/kg) and placed into a stereotaxic apparatus (David Kopf Instruments) in absence of pedal reflexes. An eye ointment was applied on the eyes to avoid drying of the corneas and a local painkiller was subcutaneously injected before opening the skin and cleaning the skull using NaCl. The stereotactic landmark bregma was identified with the help of a DINO Lit D-sub VGA microscope (VWR) and used to calculate the final stereotactic coordinates to target lobes IV/V of the cerebellum (AP: −5.63 mm, ML: 0 mm and DV: −1 and – 0.75 mm). A small hole was drilled using a micro drill (WPI) and 300 nL of AAV was injected using a 34 g beveled NanoFil needle (WPI), a 10 μL NanoFil syringe (WPI) and a microinjection pump (WPI) to control the injection speed (100 nL/min). After the injection at each depth, the syringe was kept in place for 3 min and then slowly retracted. Afterward, the skull was re-hydrated with NaCl, the wound was closed, and mice were given a dose of carprofene intraperitoneally (100 μL/10g BW) to reduce postsurgical pain. Mice were given a subcutaneous injection of 5% glucose solution (100 μL/10g BW) and placed on a hot plate (Labotect) at 37°C

to enhance postoperative recovery. 2 weeks (for AAV1/2-Ef1α-DIO EYFP injections) or 3-4 weeks (for AAV2/rh10-L7-6-EFGP-WPRE, AAV2/rh10-L7-6-EFGPP2A-Cre-WPRE or ssAAV-1/2-hEF1α-dlox-dAPEX2(rev)-dlox-WPRE-hGHp(A) injections) post-injection mice were transcardially perfused.

Multiplex fluorescent *in situ* hybridization

Transcardial perfusion and tissue processing was performed as described above ("Tissue processing and immunohistochemical analysis"). 40 μm sagittal cerebellar sections from 6-week-old mice previously injected with AAV1/2-Ef1α-DIO-EYFP were mounted on SuperFrost Ultra plus microscope slides (Thermo Scientific) and dried overnight at RT. Multiplex fluorescent RNA *in situ* hybridization was performed using RNAscope Fluorescent Multiplex Detection Reagents (323110, ACDBio, Newark, CA, USA) according to the instructions provided by the manufacturer for frozen tissue. The probe for *Grid2ip* (Mm-*Grid2ip*-C1) was designed by ACDBio (Cat No. 1253061-C1). Hybridized probe was detected with Opal 650 (PerkinElmer). Sections were mounted using ProLong Gold Antifade Mounting Medium with NucBlue Staining (Invitrogen), sealed with nail polish and imaged 24h later at a confocal microscope Stellaris (Leica) equipped with a 63× objective (HC PL APO 63x/1.30 GLYC CORR CS2, Stellaris).

Behavioral analysis

Rotarod

2-month-old AP-2 cKO mice and control littermates were acclimated to the rotarod apparatus (Ugo Basile) in a 5-min run on a rod rotating at a constant speed of 8 rpm for 2 days in a row. On the third day, the mice went through 3 test runs where they had to balance on the rotating rod for 5 min while the speed increased from 4 to 40 rpm within 5 min. Between runs, a 30 min break was kept. The duration that each mouse was able to stay on the rotating rod in each run was recorded as time to fall and used as parameter for the analysis. The time to fall was then averaged across 3 runs.

DigiGait treadmill test

The Digigait motorized transparent treadmill (Mouse Specifics, Inc.) was used to assess locomotor performance. Recording of animals from a ventral view was possible thanks to a high-speed video camera placed below the transparent belt of the motorized treadmill. 2-month-old AP-2 cKO mice and control littermates were allowed to explore the treadmill compartment the day before the actual experiment for 1 min at the speed of 8 cm/s. The day of the experiment, the speed of the belt was increased from 8 cm/s to 14, 18, 24 and 30 cm/s for video recording depending on the locomotor capability. The percentage of mice able to perform the task at each speed for each genotype was calculated and shown in the analysis as DigiGait performance.

SIMI motion test

2-month-old AP-2 cKO mice and control littermates were tested to cross beams of 1.3 m in length and 5, 12 or 25 mm wide. Individual trials were recorded through 8 high-speed cameras (mV Blue Cougar XD; 200 frames/second) strategically positioned in a circular arrangement around the beam. The camera's positioning allowed the performance capture from 8 different angles. For detailed analysis, the camera parallel to the beam was used for the 2D reconstruction of joint kinematics. Each mouse crossed every beam for a minimum of 3 times. The number of slips per run was counted and averaged across all runs. The limb kinematics of individual step cycles were normalized to account for differences in the duration of stance and swing and averaged for each mouse and then for each genotype.

Manual annotation of the step cycle and tracking using DeepLabCut on markerless animals were utilized for kinematic analysis. The manual annotation required the frame-by-frame examination of the videos to determine the beginning of the swing phase, the end of the swing phase/start of the stance phase, and the end of the stance phase. Steps resulting in footslips were excluded from the kinematic analysis, and individual steps were demarked from swing (forward propulsion of the limb) to stance (support phase) phase. Only 2 AP-2 cKO mice were analyzed for the 5 mm beam since the remaining animals were not able to cross the beam. We did not exclude any of the control mice for the narrower beam. DeepLabCut was used to track the 2D coordinates of the mice and to track the position of the beam in the video and establish the baseline for the vertical axis. The coordinates extracted by DeepLabCut were uploaded to AutoGaitA[42] to calculate angles and velocities, to normalize the coordinate across step cycles, to average trials per mouse and to average groups per genotype. The grouped values were analyzed using GraphPad Prism version 9.5.1 (GraphPad Software, Inc., USA).

Echo-MRI body composition analysis

The body composition of 2-month-old AP-2 cKO male mice and control littermates was measured using an EchoMRI-100H Body Composition Analyzer (EchoMRI). The whole-body masses of fat, lean, free water and total water were measured. Mice were placed in an animal holder and measures were taken 3 times per mouse, for a duration of 0.5–3.2 min each. The measurements were then averaged between the 3 runs and shown as percentage of body weight.

In vitro whole cell recordings

1-month-old AP-2 cKO mice and control littermates were used for recordings in acute brain slices. Animals were decapitated and the brain was rapidly placed in ice-cold artificial cerebrospinal fluid (ACSF, in mM: 124 NaCl, 2.5 KCl, 1.25 NaH_2PO_4, 26 $NaHCO_3$, 1 $MgSO_4$, 2 $CaCl_2$, 25 D-Glucose and 1mM kynurenic acid), bubbled with 95%/5% O_2/CO_2 (pH 7.4). Acute coronal 250 μm slices containing the cerebellum were prepared with a vibratome (Campden Instruments 7000smz-2), placed in warm ACSF without

kynurenic acid bubbled with 95%/5% O2/CO2 (pH 7.4), and maintained at 32°C–34°C for ~30 min, then cooled to room temperature (22°C–24°C) for at least 1 h before use. For experiments, slices were transferred to the recording chamber and superfused (2 mL.min-1) with ACSF without kynurenic acid at 32°C bubbled with 95%/5% O2/CO2 (pH 7.4). Purkinje neurons were identified with an Olympus 40× water-immersion objective. Pipettes with resistance 5–6 MΩ made of borosilicate glass capillaries with O.D. 1.5 mm, I.D. 0.86 mm (Sutter, Item# BF-150-86-10) were prepared using P-97 micropipette puller (Sutter Instruments, Item# P-97) and contained (in mM): 127 K-gluconate, 8 KCl, 10 phosphocreatine, 10 HEPES, 4 Mg-ATP, 0.3 Na-GTP (osmolality, 285 mOsm; pH 7.2 adjusted with KOH). Somatic whole-cell current-clamp recordings were made from cerebellar Purkinje neurons using Multiclamp 700B amplifier and Digidata 1550B digitizer (Molecular Devices). Data were acquired with Clampex 11.2 (Molecular Devices), digitized at 10 kHz. Electrophysiology data analysis was performed using Clampfit 11.3 (Molecular Devices).

Cerebellar acute slices

1-month-old AP-2 cKO mice and control littermates were sacrificed via cervical dislocation. Brains were isolated and cerebellum dissected. 200 μm horizontal acute slices were obtained from the cerebellum with a VT1200 Vibratome (Leica). While cutting, the cerebellum was submerged in ice-cold, carbogen saturated (95% O_2 and 5% CO_2) low-Ca^{2+} artificial cerebrospinal fluid (ACSF: 125 mM NaCl, 2.5 mM KCl, 1.25 mM sodium phosphate buffer 0.4 M, 25 mM $NaHCO_3$, 25 mM glucose, 0.5 mM $CaCl_2$ and 3.5 mM $MgCl_2$, osmolarity adjusted between 310 and 330 milliosmoles, pH = 7.4).

MG132 experiments

To test whether GRID2IP levels were changed after proteasome inhibition, cerebellar acute slices from 1-month-old AP-2 cKO and control littermates were treated with the proteasome inhibitor MG132. Slices were incubated for 6.5 h at 37°C/5% CO_2 with 100 μM MG132 or 100 μM DMSO (control) diluted in culturing medium (MEM, 0.00125% ascorbic acid, 10 mM D-glucose, 1 mM GlutaMAX; 20% (v/v) horse serum, 0.01 mg/mL insulin, 14.4 mM NaCl; 1% P/S). Afterward, slices were fixed for 1h at RT with 4% PFA before immunohistochemistry was performed.

Transferrin uptake assay in cerebellar acute slices

For transferrin (Tfn) uptake, 100 μm-thick horizontal cerebellar acute slices from 1-month-old WT and AP-2 cKO mice were obtained as described above. Slices were incubated in ACSF for 2 h at 37°C/5% CO_2 before incubation for 1 h with 25 μg/μL human Tfn conjugated to Alexa Fluor 488 (Invitrogen) in ACSF. Cell surface-bound Tfn was removed by an ice-cold acid wash (0.2 M acetic acid +0.5 M NaCl, pH 2.8) for 5 min then rinsed with ice-cold PBS 3 times. Afterward, slices were fixed for 1h at RT with 4% PFA before immunohistochemistry was performed for calbindin.

Antibody uptake assay in cerebellar acute slices with luminal domain antibody

For antibody uptake, 1-month-old AP-2 cKO mice and control littermates were sacrificed via cervical dislocation and 100 μm-thick horizontal sections were obtained as described above. Slices were incubated in ACSF for 1 h at 37°C/5% CO_2 before incubation for 1.5 h with 10 μg luminal synaptotagmin1-oyster 650 (Syt1-650; SySy) in ACSF. Cell surface-bound Syt1-650 was removed by an ice-cold acid wash (0.2 M acetic acid +0.5 M NaCl, pH 2.8) for 5 min then rinsed with ice-cold PBS 3 times. Afterward, slices were fixed for 1h at RT with 4% PFA before immunohistochemistry was performed for calbindin as a Purkinje cell marker and total synaptotagmin1. Fluorescent signal of luminal Syt1 and total Syt1 in Purkinje cells was measured after background subtraction and the ratio of luminal/total was used as a readout of antibody uptake.

FM1-43FX dye assay in cerebellar acute slices

For FM1-43FX dye, 100 μm-thick horizontal cerebellar acute slices from 1-month-old WT and AP-2 cKO mice were obtained as described above. Slices were incubated in ACSF for 30 min at 37°C/5% CO_2, then incubated in 10 μM FM1-43FX dye (in ACSF) for 2 min at RT followed by an electrical stimulation with 100 APs at 100 Hz using an RC-47FSLP stimulation chamber (Warner Instruments). To monitor activity-based endocytosis, slices were kept in ACSF containing 10 μm μM FM1-43FX dye for 10 more minutes and then washed 3 times in ACSF. Afterward, slices were fixed for 1h at RT with 4% PFA, washed 3 times in 1x PBS before immunohistochemistry for Purkinje cell marker calbindin was performed. Mean gray value was used as a readout for fluorescence level of FM1-43FX dye in Purkinje cells after background subtraction.

Primary cerebellar culture

Culture preparation

Postnatal day 8 (P8) AP-2 cKO pups and control littermates were decapitated and brains were collected in ice-cold solution B (300 mg BSA (fatty acid free), 1.5mM MgSO4 and 13 mM glucose in 100 mL dPBS). The cerebellum was isolated and chopped into 700 μm thick pieces with a tissue chopper (Cavey Laboratory Engineering Co. LTD). The chopped tissue was subsequently incubated in solution T (solution B plus 1mg/4mL trypsin) at 37°C/5% CO_2 for 15 min. In order to stop trypsinization, solution C (600U DNase; 0.5 mg Soybean Trypsin Inhibitor (SBTI); 100 μL $MgSO_4$ in 10 mL solution B) was added to the samples (twice the volume as solution T), which were then centrifuged at 1000g for 1 min at 4°C. The supernatant was removed and cell suspension was dissolved in 1 mL growth medium (5 mL FBS in 50 mL stock medium: 500 mL DMEM; 2 mL B-27, 0.74 g KCl, 10 mM glucose, 1 mM

sodium pyruvate, 5 mL P/S). Afterward, the cell suspension was mechanically dissociated with a fire-polished glass pipette. Dissociated cells were layered on top of 5 mL EBSS (EBSS plus % (w/v) bovine serum albumin (BSA); 3 mM 3.82% MgSO4) and centrifuged at 1500 g for 5 min at 4°C. Afterward, the supernatant was discarded and the pellet dissolved in growth medium and cell density determined using a Neubauer counting chamber. Finally, cells were plated at a density of 750000 cells per coverslip and fed after 1 h with growth medium. After 24h, half of the medium was replaced with fresh growth medium plus 4 μM AraC. Cerebellar neurons were cultured for 19 days (DIV 19) under constant conditions at 37°C/5% CO_2.

Primary cerebellar culture viral transduction

In order to identify Purkinje cells in primary cerebellar cultures, neurons were transduced on DIV3 with AAV2/rh10-L7-6-EFGP-WPRE (titer 5.05 *10^{13} GC/mL).

PitStop2-mediated CME inhibition

On DIV18, primary cerebellar cultures from WT mice were incubated with 30μM PitStop2 (Abcam) or DMSO (control) diluted into cerebellum growth medium at 37°C/5% CO_2 for 24h. Afterward, neurons were fixed at DIV19 with 4% PFA for 10 min at RT and used for experiments.

Transferrin uptake assay

For transferrin uptake, cerebellar growth medium was removed from DIV19 primary cerebellar cultures from AP-2 cKO mice and control littermates (previously transduced with AAV2/rh10-L7-6-EFGP-WPRE) and replaced with pre-warmed Neurobasal-A Medium (Thermo Fisher Scientific). Neurons were starved in this medium for 2h at 37°C/5% and then incubated for 30 min at 37°C/5% with the same medium containing 15 μg/mL human Transferrin conjugated to Alexa Fluor 568 (BioTrend). Cell-surface bound Transferrin was removed by 3 PBS washes and immediately fixed with 4% PFA for 10 min at RT.

Transferrin uptake was also used to prove CME inhibition by Pitstop2 in WT primary cerebellar culture. For this purpose, DIV18 neurons were incubated with 30μM Pitstop2 (Abcam) or DMSO (control) diluted into cerebellum growth medium at 37°C/5% CO_2 for 24h. On DIV19, neurons were starved for 2h at 37°C/5% in a pre-warmed Neurobasal-A medium containing 30μM Pitstop2. Afterward, 15 μg/mL human Transferrin conjugated to Alexa Fluor 488 were added to the medium for 30 min at 37°C/5%. Cell-surface bound Transferrin was removed by 3 PBS washes and immediately fixed with 4% PFA for 10 min at RT.

Immunocytochemistry

Fixed primary cerebellar cultures were blocked for 1h at RT in 0.3% saponin (Sigma) in PBS plus 5% NGS. Afterward, cells were incubated for 1h at RT with primary antibodies (see Key Resource Table) diluted in 0.3% saponin/PBS plus 5% NGS. Cells were washed 3 times with PBS and then incubated for 30 min at RT with secondary antibodies (see Key Resource Table) diluted in 0.3% saponin/PBS plus 5% NGS. Finally, cells were washed 3 times with PBS and coverslips were mounted on glass slides with Immu-Mount (Epredia).

Cerebellar organotypic cultures (OTCs) from p8 pups

OTCs preparation

P8 AP-2 cKO pups and control littermates were decapitated and brains were collected in ice-cold HBSS (Gibco). Cerebellum was isolated and 300 μm sagittal slices were obtained with a tissue chopper (Cavey Laboratory Engineering Co. LTD). Sections were collected and washed 3 times by being carefully transferred with a glass pipette in 3 separate dishes containing pre-warmed HBSS. Afterward, slices were transferred onto Millicell Standing Cell Culture Inserts (Merk Millipore) and fed with culturing medium (MEM, 0.00125% ascorbic acid, 10 mM D-glucose, 1 mM GlutaMAX, 20% (v/v) horse serum, 0.01 mg/mL insulin, 14.4 mM NaCl, 1% P/S) from below the cell culture insert membrane. Every 2 days, the medium was replaced and slices were cultured for 21 days under constant conditions at 37°C/5% CO_2.

OTCs viral transduction

For calcium imaging, OTCs were transduced at DIV1 by applying 1 μL of ssAAV-9/2-mCaMKIIα-jGCaMP7f-WPRE-bGHp(A) (titer 1.1x10^{13}, Viral vector facility Zurich) on top of each slice. Slices were cultured until DIV21 at 37°C/5% CO_2 until they were used for experiments.

Ceftriaxone treatment

OTCs from AP-2 cKO mice and control littermates previously transduced with ssAAV-9/2-mCaMKIIα-jGCaMP7f-WPRE-bGHp(A) were cultured for 15 days in OTC culturing medium at 37°C/5% CO_2. On DIV 15, slices were treated with 100 μM Ceftriaxone for 7 consecutive days until DIV21. On DIV21, OTCs were either used for calcium imaging experiments or shock-frozen in liquid nitrogen and stored at −80°C until tissue lysis for immunoblotting analysis. Untreated OTCs were used as control.

Calcium imaging experiments

DIV 21 OTCs from AP-2 cKO mice and control littermates were used for GCaMP7f-based calcium imaging. Slices were cut out from the cell culture inserts and placed into an RC-47FSLP stimulation chamber (Warner Instruments) filled with OTC imaging medium (2 mM $CaCl_2$, 10 mM D-glucose, 3 mM KCl, 1 mM $MgCl_2$, 136 mM NaCl, 24 mM $NaHCO_3$, 1.25 mM NaH_2HPO_4 in dH_2O) bubbled

with 95%/5% O_2/CO_2 and constantly perfused. A Multiphoton microscope SP8 (Leica) equipped with a 20x/0.75 multi-immersion objective was used for confocal live imaging. 60s recordings (1–3 recording per slice) were acquired at 512x512 pixel resolution, bidirectional at 1 frame per second. After 20s of baseline recording, slices were stimulated once with a 100 Hz pulse and recorded for 40 more seconds, for a total of 60s for each recording.

Calcium imaging analysis

Cell/dendritic patches detection and signal extraction

Signal extraction from calcium imaging recordings was done using ImageJ (Fiji). Region of interests (ROIs) were drawn around Purkinje cell bodies or dendritic patches identified thanks to GFP expression driven by the ssAAV-9/2-mCaMKIIα-jGCaMP7f-WPRE-bGHp(A) virus. The mean gray value from each ROI was extracted for every single frame (60 in total) and used for the analysis.

Automatic cell curation and filtering

Ca^{2+} signals were sampled at a rate of 1 Hz. Individual Ca^{2+}transients were normalised to the 5 s-period preceding electrical stimulation. To identify low quality components, we performed k-means clustering (k = 5, nsets = 20, kmeans function, stats package, R). The number of clusters was optimised according to the total within-cluster sum of squared distances. We identified a distinct cluster of low-quality components with continuous baseline shifts, indicative of motion artifacts or bleaching. Components in this cluster were discarded from further analysis (11–19% of the total). All other components were used for further analysis.

Characterization of stimulus responses

Heatmaps. For visual inspection of Ca^{2+} transients in the form of activity maps, individual transients were smoothed (Tukey's smoothing with running median of 3, smooth function, stats package, R), sorted according to the median signal amplitude of the 10 s-period following stimulation.

Individual response parameters. The following parameters were used to assess stimulus responses of individual components.

Parameter	Description
Average Ca^{2+} response	Arithmetic mean of the Ca^{2+} signal within the 10 s-period following electrical stimulation
Peak Ca^{2+} response	Highest Ca^{2+} signal within the 40 s-period following electrical stimulation
Time to peak	Time point of the maximum Ca^{2+} response within the 40 s-period following electrical stimulation

Synchronicity. To assess the degree of similarity in firing patterns of individual Ca^{2+} transients, we calculated the pairwise Pearson correlation coefficient for each component with all other components within the 40 s-period following electrical stimulation per genotype and condition. For visual inspection, the correlation matrix per genotype and condition was sorted according to hierarchical cluster analysis (cor_sort function, correlation package, and hclust function, stats package, R).

OTCs from 1-month-old animals

1-month-old AP-2 cKO mice and control littermates were sacrificed and brains were collected in ice-cold HBSS (Gibco). Cerebellum was isolated and 300 μm horizontal sections were obtained with a VT1200 Vibratome (Leica). Sections were collected and washed 3 times by being carefully transferred with a glass pipette in 3 separate dishes containing pre-warmed HBSS. Afterward, slices were transferred onto Millicell Standig Cell Culture Inserts (Merk Millipore) and fed with culturing medium (MEM, 0.00125% ascorbic acid, 10 mM D-glucose, 1 mM GlutaMAX, 20% (v/v) horse serum, 0.01 mg/mL insulin, 14.4 mM NaCl, 1% P/S) from below the cell culture insert membrane. Every 2 days, the medium was replaced and slices were cultured for 14 days under constant conditions at 37°C/5% CO_2 in OTC culturing media either with vehicle or 100 μM ceftriaxone. OTCs were then fixed in 4% PFA and stained for calbindin (see IHC above). Purkinje cell density was determined based on calbindin signal.

Image acquisition

Images of fluorescently stained brain slices, primary cerebellar cultures and adult OTCs were acquired at a confocal microscope Stellaris (Leica) or at a confocal microscope SP8 (Leica). At 20x (HC PL APO 20x/0.75 CS2, Stellaris) magnification, single plane tile images were acquired for stained brain slices. At 40x (HC PL APO 40x/0.95 CORR, Stellaris; PL Apo 40x/0.85 CORR CS, SP8) and 63x (HC PL APO 63x/1.30 GLYC CORR CS2, Stellaris; PL Apo 63x/1.40 Oil CS2, SP8) either single plane images or z-stacks were acquired for both stained brain slices and primary neurons. Z-stacks are shown as maximum intensity projection images. Tile images were merged with LAS X software (Leica).

In situ hybridized sections were imaged at a confocal microscope Stellaris (Leica) equipped with a 63× objective (HC PL APO 63x/1.30 GLYC CORR CS2, Stellaris). Z-stacks were acquired and images are shown as maximum intensity projection of z stack.

Brightfield images were acquired with a slide scanner microscope (S360 Hamamatsu) equipped with a 40× objective.

VGAT surface levels analysis on perfused brain sections

Brain sections were obtained from perfused mice as described above (Tissue processing and immunohistochemical analysis). For immunofluorescent staining, brain sections were washed once in PBS for 10 min and incubated in blocking solution containing 10% normal goat serum (NGS) in PBS followed by incubation in primary antibody for the luminal domain (anti-VGAT-Oyster 550) for 2h at room temperature (RT). Afterward sections were postfixed in 2% PFA for 15 min and washed in 1x PBS 3 times. Sections were then incubated in blocking solution containing 10% normal goat serum (NGS) in PBS plus 0.5% Triton X-100 (0.5% PBT) for 1h at room temperature. Sections were incubated with primary antibodies for cytosolic domains for 48 h at 4°C in 0.3% PBT plus 3% NGS and afterward washed 3 times for 5–10 min each in 0.3% PBT. Sections were then incubated with secondary antibodies for 2h in the dark at RT in 0.3% PBT plus 3% NGS and washed 3 times for 5–10 min each in 0.3% PBT. Sections were finally mounted on gelatin-coated glass slides with Immu-Mount (Epredia). The following primary antibodies dilutions were used: 1:500 for mouse anti-Calbindin, 1:300 for guinea pig anti-VGAT and 1:200 for rabbit anti-VGAT-Oyster550. All Alexa fluorophore-conjugated secondary antibodies were used at a 1:500 dilution. Fluorescent signal of luminal VGAT-Oyster550 and total VGAT in Purkinje cells was measured after background subtraction and the ratio of luminal/total was used as a readout of surface VGAT in Purkinje cells.

Analysis of fluorescently stained brain slices

The following analysis was used to quantify GRID2IP levels in 200 μm thick cerebellar sagittal acute slices treated with MG132 or DMSO, GLURδ2 levels in distal dendrites and AP-2α/μ in Purkinje cell somata in 40 μm thick sagittal cerebellar slices as well as transferrin-uptake in 100 μm thick cerebellar sagittal acute slices. The mean gray value of the GRID2IP, or transferrin signal in Purkinje cell somata or GLURδ2 in distal dendrites was extracted with ImageJ (Fiji) and normalized for background fluorescence (area devoid of GRID2IP, GLURδ2, or transferrin-488 signal). In fluorescently stained brain slices, mean gray value for AP-2μ staining was extracted with ImageJ (Fiji) either in Purkinje cells or FoxP2-positive inferior olive nuclei and normalized for background fluorescence.

Analysis of *in situ* hybridized sections

For analysis of *Grid2ip* mRNA puncta, maximum intensity projections of acquired z stack were generated for both RNAscope probe and GFP (AAV1/2-Ef1α-DIO EYFP) channels using ImageJ (Fiji). The GFP fluorescence mediated by the AAV transduction of Purkinje cells was used to draw ROIs including both Purkinje cells somata and dendrites. These same ROIs were copied onto the *Grid2ip* channel and allowed to mark the region where RNA puncta were quantified. For this purpose, a threshold was set on the channel showing *Grid2ip* mRNA expression, allowing to label exclusively the signal coming from mRNA puncta. Puncta where finally quantified using the particle analysis tool in Fiji and the total number of puncta was normalized by the ROI area for each single image.

Cell number quantification

Cresyl-violet stained sagittal cerebellar sections from 1-, 2- and 3-month-old mice were used to quantify the number of Purkinje cells in AP-2 cKO mice and control littermates. Cerebellar lobes from lobe I to lobe X were identified in 3–5 sections from each mouse, ranging from bregma 0.48 mm to bregma 1.2 mm according to the Allen Brain Atlas. Purkinje cell number was counted in each lobe for each bregma coordinate and then averaged, in order to obtain the total number of neurons per lobe. Aperio Image Scope image viewing software (Leica) was used to analyze acquired images.

Analysis of perisomatic puncta

Perisomatic quantification of vGLUT2 and vGLUT1 puncta was performed on fluorescently immunostained sagittal cerebellar sections from WT and AP-2 cKO 1- and 3-month-old animals. z stack confocal images were acquired at a 63× magnification and maximum intensity projections extracted from these stacks were used for this analysis. Using ImageJ, the GFP fluorescence mediated by the AAV transduction or the tdTomato fluorescence of Purkinje cells was used to draw ROIs around somata. The number of puncta per cell was quantified and normalized to the area of the soma and used for further statistical analysis.

Colocalization analysis

Colocalization analysis between AP-2α and GRID2IP was performed on fluorescently immunostained sagittal cerebellar sections from 2-month-old WT mice. Non-processed raw dual channel images were used for the analysis. ROIs were manually drawn in order to outline somata, primary or secondary dendrites. Pearson's correlation coefficient (Rp) was determined using the JACoP plug-in in ImageJ. The same analysis was performed to investigate differences in colocalization between GLURδ2 and VGLUT1 in distal Purkinje cell dendrites of 1month-old AP-2 cko mice and control littermates.

Analysis of number of spines

The number of spines in proximal and distal dendrites was quantified in sagittal cerebellar sections from 6-week-old AP-2 cKO mice and control littermates previously injected with AAV1/2-Ef1α-DIO EYFP. z stack confocal images were acquired at a 63× magnification and single planes extracted from these stacks were used for this analysis. Using ImageJ, a 10 μm line was drawn and the number of spines was counted within this length. 4 to 7 Purkinje cells per mouse were analyzed. For each cell, 3 different measurements

were obtained and then averaged for final analysis. The same quantification was performed to determine differences in number of spines in Purkinje cells from 10-week-old AP-2m1$^{flox/flox}$ mice previously injected with AAV2/rh10-L7-6-EFGP-WPRE control virus or AAV2/rh10-L7-6-EFGP-P2A-Cre-WPRE virus to obtain AP-2μ acute deletion in the adult cerebellum.

AMIRA-based 3D reconstruction and analysis

40 μm sagittal cerebellar sections from 6-week-old AP-2 cKO mice and littermates previously injected with AAV1/2-Ef1α-DIO EYFP or AAV2/rh10-L7-6-EFGP-WPRE/AAV2/rh10-L7-6-EFGPP2A-Cre-WPRE were stained for GFP and co-stained for GRID2IP/VGLUT1/VGLUT2 and used for the analysis. Images were acquired using HC PL APO 63x/1.30 GLYC CORR CS2 objective at a resolution of 1024× 1024 pixels in sequential scanning frame-by-frame mode. Stacks of 50–80 optical sections were acquired, with a fixed stack size of 0.25 μm. 3D reconstructions were generated with Amira Software 2020.2 (Thermo Fisher Scientific). First, the surface area of single GFP-positive Purkinje cell (soma and dendrites) was reconstructed using the Amira segmentation editor. GRID2IP/VGLUT1/VGLUT2 signal was defined by generating the isosurface. Afterward, the surface of '300-nm-distant' GRID2IP/VGLUT1/VGLUT2-positive voxels was mapped onto GFP-positive reconstructed cell using the "surface distance" tool and extracted as a histogram. Values extracted from the histogram (number of voxels/μm^2) were plotted and used for colocalization analysis.

QUANTIFICATION AND STATISTICAL ANALYSIS

Statistical analyses were conducted on mice values or cell values (indicated by data points, "n") from at least a group of 3 mice per genotype or at least 3 independent experiments (indicated by "N", biological replicates), if not stated otherwise in the figure legend. MS Excel (Microsoft, USA) and GraphPad Prism version 9.5.1 (GraphPad Software, Inc., USA) were used for statistical analysis and result illustration (unless otherwise stated). Unpaired t test or Welch's unpaired t test were used to compare the means of two groups. Statistical analysis of normalized data between the two groups was performed using a one-tailed unpaired Student's t test. Two-tailed Mann-Whitney test was used for analysis between two groups for non-normally distributed non-normalized data (i.e., number of spikes evoked by intracellular current injection). Statistical difference between more than two groups were compared with one-way ANOVA (Tukey's posthoc test for multiple comparison was used to determine the statistical significance between the groups). Statistical difference between more than two groups and two conditions was evaluated using two-way ANOVA with Šidák post-hoc test. Significant differences were accepted at $p \leq 0.05$ indicated by asterisks: $^{*}p \leq 0.05$; $^{**}p \leq 0.01$; $^{***}p \leq 0.001$ and $^{****}p \leq 0.0001$.